© 2015. Published by The Company of Biologists Ltd | Development (2015) 142, 2026-2036 doi:10.1242/dev.119248

RESEARCH ARTICLE

The cytoskeleton-associated protein SCHIP1 is involved in axon guidance, and is required for piriform cortex and anterior commissure development

Esther Klingler[1,2,3,*], Pierre-Marie Martin[1,2,3,‡,§], Marta Garcia[1,2,3,§], Caroline Moreau-Fauvarque[2,4,5], Julien Falk[6], Fabrice Chareyre[7], Marco Giovannini[8], Alain Chédotal[2,4,5], Jean-Antoine Girault[1,2,3] and Laurence Goutebroze[1,2,3,¶]

ABSTRACT

SCHIP1 is a cytoplasmic partner of cortical cytoskeleton ankyrins. The IQCJ-SCHIP1 isoform is a component of axon initial segments and nodes of Ranvier of mature axons in peripheral and central nervous systems, where it associates with membrane complexes comprising cell adhesion molecules. SCHIP1 is also expressed in the mouse developing central nervous system during embryonic stages of active axonogenesis. Here, we identify a new and early role for SCHIP1 during axon development and establishment of the anterior commissure (AC). The AC is composed of axons from the piriform cortex, the anterior olfactory nucleus and the amygdala. *Schip1* mutant mice displayed early defects in AC development that might result from impaired axon growth and guidance. In addition, mutant mice presented a reduced thickness of the piriform cortex, which affected projection neurons in layers 2/3 and was likely to result from cell death rather than from impairment of neuron generation or migration. Piriform cortex neurons from E14.5 mutant embryos displayed axon initiation/outgrowth delay and guidance defects *in vitro*. The sensitivity of growth cones to semaphorin 3F and Eph receptor B2, two repulsive guidance cues crucial for AC development, was increased, providing a possible basis for certain fiber tract alterations. Thus, our results reveal new evidence for the involvement of cortical cytoskeleton-associated proteins in the regulation of axon development and their importance for the formation of neuronal circuits.

KEY WORDS: Anterior commissure, Piriform cortex, SCHIP1, Axon growth and guidance, SEMA3F, EPHB2

INTRODUCTION

During nervous system development, axon outgrowth and guidance are key processes for the proper formation of neuronal circuits. Schwannomin-interacting protein 1 (SCHIP1) is a cytoplasmic protein identified as a partner of the tumor suppressor protein schwannomin [also known as merlin or neurofibromatosis 2 (NF2)] (Goutebroze et al., 2000). The IQCJ-SCHIP1 isoform is a component of axon initial segments and nodes of Ranvier, two regions highly enriched in Na_v channels important for the initiation and the saltatory conduction of action potentials, respectively (Martin et al., 2008). In these regions, Na_v channels sit in multimolecular complexes comprising KCNQ channels and cell adhesion molecules (CAMs), NRCAM and neurofascin, anchored to the actin cytoskeleton through their interaction with the $ankyrin_G$/βIV spectrin-based cortical cytoskeleton (Buttermore et al., 2013). In this complex, SCHIP1 interacts directly with $ankyrin_G$ (also known as ankyrin 3) (Martin et al., 2008). SCHIP1 is also able to interact with $ankyrin_B$ (also known as ankyrin 2), which binds adhesion molecules involved in axon formation (Bennett and Lorenzo, 2013). $Ankyrin_B$ regulates both axon elongation and navigation (Colavita and Culotti, 1998; Gil et al., 2003; Kunimoto and Suzuki, 1995; Nishimura et al., 2003), although its precise *in vivo* contribution is poorly characterized (Scotland et al., 1998).

The *Schip1* gene is expressed in the brain during stages of active axonogenesis (http://www.genepaint.org/cgi-bin/mgrqcgi94) suggesting that it could function in axon outgrowth and/or navigation. Using a gene-trap strategy, previous studies revealed the consequences of SCHIP1 loss of function on embryonic development, but did not investigate specific morphological brain abnormalities in mutant mice (Chen et al., 2004; Schmahl et al., 2007, 2008). It is noteworthy that the gene-trap sequence was introduced into the *Schip1* gene at a position where it was expected to alter the expression of two isoforms (SCHIP1a and IQCJ-SCHIP1) only.

In the present study, we investigated the role of SCHIP1 in brain development by generating *Schip1*Δ10 mutant mice, which are impaired in the expression of all *Schip1* isoforms. We show that *Schip1*Δ10 mice display a partial agenesis of the anterior commissure (AC). The piriform cortex, characterized by its three-layered organization, is one of the main sources of AC axons (de Castro, 2009) and plays key roles in odor discrimination, association and learning (Bekkers and Suzuki, 2013). Multiple guidance signals are known to be expressed in the piriform cortex and surrounding regions and to control the development of the AC, including ephrin, netrin and semaphorin family members (Lindwall et al., 2007).

Using a combination of *in vivo* and *in vitro* approaches, we show that *Schip1*Δ10 mice display decreased thickness of the piriform cortex, which may result from cell death, and early AC axon developmental defects, which are likely to be associated with impaired axon elongation and guidance. Our results further suggest that the *Schip1*Δ10 mutation changes axon sensitivity to the repulsive guidance cues semaphorin 3F (SEMA3F) and Eph receptor B2 (EPHB2), which are known to participate in AC formation (Henkemeyer et al., 1996; Sahay et al., 2003).

[1]INSERM, UMR-S 839, Paris F-75005, France. [2]Sorbonne Universités, UPMC Univ Paris 06, Paris F-75005, France. [3]Institut du Fer à Moulin, Paris F-75005, France. [4]Institut de la Vision, INSERM, UMR-S 968, Paris F-75012, France. [5]CNRS, UMR 7210, Paris F-75012, France. [6]Université Claude Bernard Lyon 1, CNRS, UMR 5534, CGphiMC, Lyon F-69622, France. [7]House Research Institute, Center for Neural Tumor Research, Los Angeles, CA 90095-1624, USA. [8]Department of Head and Neck Surgery, David Geffen School of Medicine, UCLA, Los Angeles, CA 90027, USA.
*Present address: Department of Basic Neurosciences, University of Geneva, Geneva, Switzerland. ‡Present address: Department of Psychiatry, University of California, San Francisco, CA, USA.
§These authors contributed equally to this work

¶Author for correspondence (laurence.goutebroze@inserm.fr)

Received 31 October 2014; Accepted 10 April 2015

Development (2015) 142, 2026-2036 doi:10.1242/dev.119248

RESULTS

Generation and characterization of *Schip1*Δ10 mice

The *Schip1* gene encodes six isoforms expressed in the mouse brain (supplementary material Fig. S1A). All isoforms differ in their N-terminus and share a C-terminal domain encoded by exons 9 to 14. This domain includes a ∼40 residue leucine zipper that is predicted to adopt a coiled-coil conformation and is required for ankyrin and schwannomin binding (Goutebroze et al., 2000; Martin et al., 2008). Mutant mice were generated by deletion of *Schip1* exon 10, which is predicted to result in a frameshift that creates a STOP codon in exon 11 (supplementary material Fig. S1B,C). We checked whether this led to the expression of truncated proteins lacking the conserved C-terminal domain common to all isoforms (supplementary material Fig. S1D-F). Immunoprecipitation experiments followed by immunoblotting using different combinations of SCHIP1 antibodies did not reveal any truncated proteins in brain extracts (supplementary material Fig. S1F and Fig. S2). Homozygous mutant mice (termed Δ10) born from heterozygous crossings were fertile and survived as long as wild-type (WT) mice (>2 years), although they suffered from a mild growth delay from birth to adulthood (data not shown).

*Schip1*Δ10 adult mice display axon tract abnormalities, which are particularly severe in the AC

Although the global anatomy of adult mutant brains did not differ from that of WT littermates, histological analyses revealed white matter defects in the AC and to a lesser extent in the corpus callosum (CC) (Fig. 1). The AC is formed by two main branches. The anterior

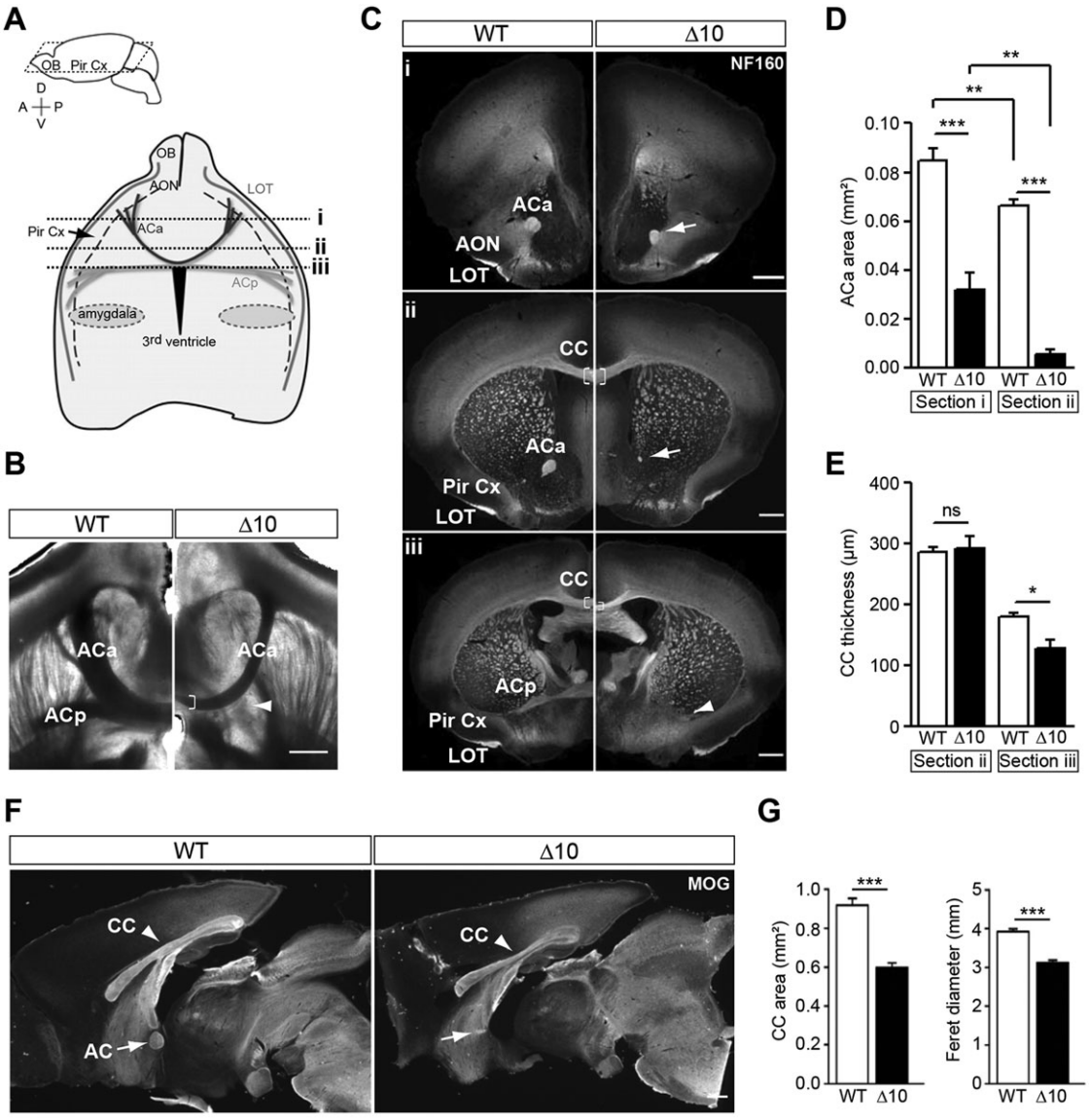

Fig. 1. *Schip1*Δ10 adult mice display fiber tract defects that are particularly severe in the AC. (A) AC organization in a horizontal section sketched on a brain lateral view (top left). OB, olfactory bulb; AON, anterior olfactory nucleus; LOT, lateral olfactory tract; Pir Cx, piriform cortex; ACa, anterior branch of the AC; ACp, posterior branch of the AC. Dashed lines, boundaries of the piriform cortex; dotted lines, levels of coronal sections (i-iii) presented in C. (B) Phase-contrast images of 500 µm-thick horizontal brain sections. Square brackets, ACa; arrowhead, absence of ACp in Δ10. (C) Coronal sections from rostral to caudal brain regions immunolabeled for neurofilament (NF160). Arrows, ACa; arrowhead, absence of ACp in Δ10; square brackets, corpus callosum (CC). (D) Quantification of ACa area in C. (E) Quantification of CC thickness at the midline in C. (F) Mid-sagittal brain sections immunolabeled for MOG. Arrows, AC; arrowheads, CC. (G) Quantification of CC area and Feret diameter. Data are mean±s.e.m. *n*=3 animals/genotype (B-E), *n*=3 sections/animal (C-E); *n*=3 animals/genotype, *n*=3-4 sections/animal (F,G). Two-way ANOVA (D,E), *t*-test (G); **P*<0.05, ***P*<0.01, ****P*<0.001; ns, not significant. Scale bars: 500 µm.

Development (2015) 142, 2026-2036 doi:10.1242/dev.119248

branch (ACa) is composed of axons from the anterior olfactory nucleus (AON) and the anterior piriform cortex, whereas the posterior branch (ACp) is composed of axons from the posterior piriform cortex and the amygdala (Cummings et al., 1997; Pires-Neto and Lent, 1993) (Fig. 1A). Horizontal sections showed a severe decrease in ACa thickness and an absence of ACp in all mutants (Fig. 1B). Serial coronal sections labeled with neurofilament antibodies confirmed these observations, showing a reduced ACa bundle area in mutants compared with WT sections. This decrease was more severe in the ACa caudal region (Fig. 1Ci,ii,D). The phenotype was even more striking for the ACp, which was missing in all mutants (Fig. 1Ciii). In caudal regions, mutant mice also displayed a thinner CC at the midline compared with WT mice (Fig. 1Ciii,E). Mid-sagittal brain sections further showed a decreased CC length along the rostrocaudal axis (Fig. 1F,G). These observations suggested a reduction of the number of axons in the CC and the ACa, and an absence of ACp axons in Δ10 mutants.

Early development of AC axons is altered in *Schip1*Δ10 embryos

To identify the origin of axonal tract defects in mutants, we studied the development of the AC, which was more severely affected than the CC. The AC starts to develop between E13.5 and E14.5, with pioneer L1CAM-immunopositive axons detected at the midline at E14.5 (Schneider et al., 2011). We therefore immunolabeled serial coronal sections of E13.5 and E14.5 brains with L1CAM antibodies (Fig. 2A,B). At E13.5, the first ACa pioneer axons were visible in WT brains, whereas they were not detectable in mutants, whatever the section plane (Fig. 2A). Moreover, at E14.5 no AC axons were detected at the midline in mutants (Fig. 2B). These results suggested that SCHIP1 is important for early AC development.

To further characterize the AC defects, we immunolabeled serial horizontal sections from E16.5 brains with L1CAM antibodies. In WT embryos, both AC branches were fully developed as previously shown by Schneider et al. (2011). By contrast, E16.5 mutant embryos displayed thinner ACa tracts (Fig. 2C) with axons that never reached the midline. Selecting specific mutant horizontal sections in which the ACa axons were closest to the midline, we determined that ACa axons terminated 432±142 µm from the midline (mean±s.e.m., n=4 Δ10 embryos). The ACp tract was absent in all mutant embryos. Very few axons arose from the posterior piriform cortex and seemed stunted, often misprojecting to rostral regions (Fig. 2C).

We further performed tracing experiments with DiI (as sketched in Fig. 2Da) to determine whether AC axons of mutant embryos misprojected towards other brain regions. In serial horizontal slices of WT DiI-injected brains, both ACa and ACp axons crossed the midline and projected towards the contralateral hemisphere. By contrast, mutant ACa labeled axons appeared less numerous and stopped before crossing the midline without aberrant projections to other regions (Fig. 2Db). Labeled axons from the posterior piriform cortex were very rare in mutant embryos and stopped growing close to the rostral ipsilateral cortex instead of projecting to the midline (Fig. 2Dc). Altogether, these observations (as summarized in Fig. 2E) suggested that SCHIP1 could contribute to AC formation by playing a role in both axon outgrowth and guidance of projecting neurons.

*Schip1*Δ10 mice display thinner projection neuron layers in the piriform cortex from E16.5, with increased cell death at E14.5

ACp axons arise mainly from the piriform cortex and the amygdala (Huang et al., 2014). This prompted us to ask whether these structures were affected in Δ10 mutants. The areas of the lateral and the basolateral nuclei of the amygdala were similar in adult Δ10 and WT mice (supplementary material Fig. S3), suggesting that the amygdala was not affected in mutants. We also analyzed the overall thickness of the piriform cortex from E14.5 to adulthood in Cresyl Violet-stained coronal sections. We defined as anterior the piriform cortex at the level of the ACa along the rostrocaudal axis (Fig. 3A, ANT) and defined as posterior the piriform cortex at the level of the ACp (Fig. 3A, POST). The thickness of the mutant anterior piriform cortex was not significantly affected during development (Fig. 3B). By contrast, from E16.5 on, the posterior piriform cortex was thinner in the mutant than in WT brains (Fig. 3B). This was not the case for the neocortex (supplementary material Table S1). Since AC axons start to grow at E13.5 (Schneider et al., 2011), and as the AC is fully established by E16.5 in mice, these results showed that the defect in posterior piriform cortex thickness coincided with the completion of AC development.

We further characterized the three-layered organization of the piriform cortex and analyzed the thickness of each layer. In WT and mutant embryos, the layers were not distinguishable at E14.5. From E16.5 on, the piriform cortex started to organize into three distinct layers with increased cell density in layer 2, even though the precise layer delimitations remained poorly defined (data not shown). At P0, the three layers were clearly distinct (Fig. 3C). Both layer 2 and layer 3 were thinner in the mutant than in the WT posterior piriform cortex (Fig. 3D). Decreased thickness was restricted to layer 2 in the anterior piriform cortex (Fig. 3D), which may account for the undetectable overall thickness reduction (Fig. 3B).

We then attempted to identify the origins of layer 2 defects. Confocal imaging of serial coronal sections stained with DAPI showed no difference in cell density between mutant and WT newborn mice (supplementary material Table S2). Hence, the reduced thickness of the layers was likely to result from an overall decrease in cell number. Layer 2 contains pyramidal cells, which are mostly generated at E12.5 (Sarma et al., 2011). BrdU injection in pregnant females at E12.5 showed no difference in the density of BrdU-immunopositive cells between WT and mutant piriform cortices at E14.5 (supplementary material Table S3), suggesting that the early migration of mutant neurons was not affected and that neurons whose axons initially form the AC were present in normal numbers in mutant piriform cortex at this stage. Also, no difference in BrdU-immunopositive cell density could be detected in layer 2 between WT and mutant at E18.5 (supplementary material Table S3). However, since layer 2 could clearly be distinguished and was already thinner in mutants at this stage (supplementary material Table S3), this indicated that a population of projecting cells disappeared between E14.5 and E18.5. Immunolabeling for cleaved caspase 3 on serial sections showed increased cell death at E14.5 in mutant compared with WT piriform cortices, which was not the case in the neocortex (Fig. 3E,F). The increased cell death in mutants was more pronounced in the posterior than in the anterior piriform cortex (Fig. 3E,F), consistent with the more severely decreased thickness observed in the posterior piriform cortex at later embryonic stages.

SCHIP1 plays a role in axon initiation and outgrowth

Altogether, our results suggested that SCHIP1 could play specific roles in the development of piriform cortex neurons *in vivo*. *In situ* hybridization of WT coronal brain sections indeed confirmed that *Schip1* is expressed in the piriform cortex during brain development at E13.5, E14.5 and P0 (supplementary material Fig. S4A). Interestingly, at P0, *Schip1*-expressing cells were mainly localized

Development (2015) 142, 2026-2036 doi:10.1242/dev.119248

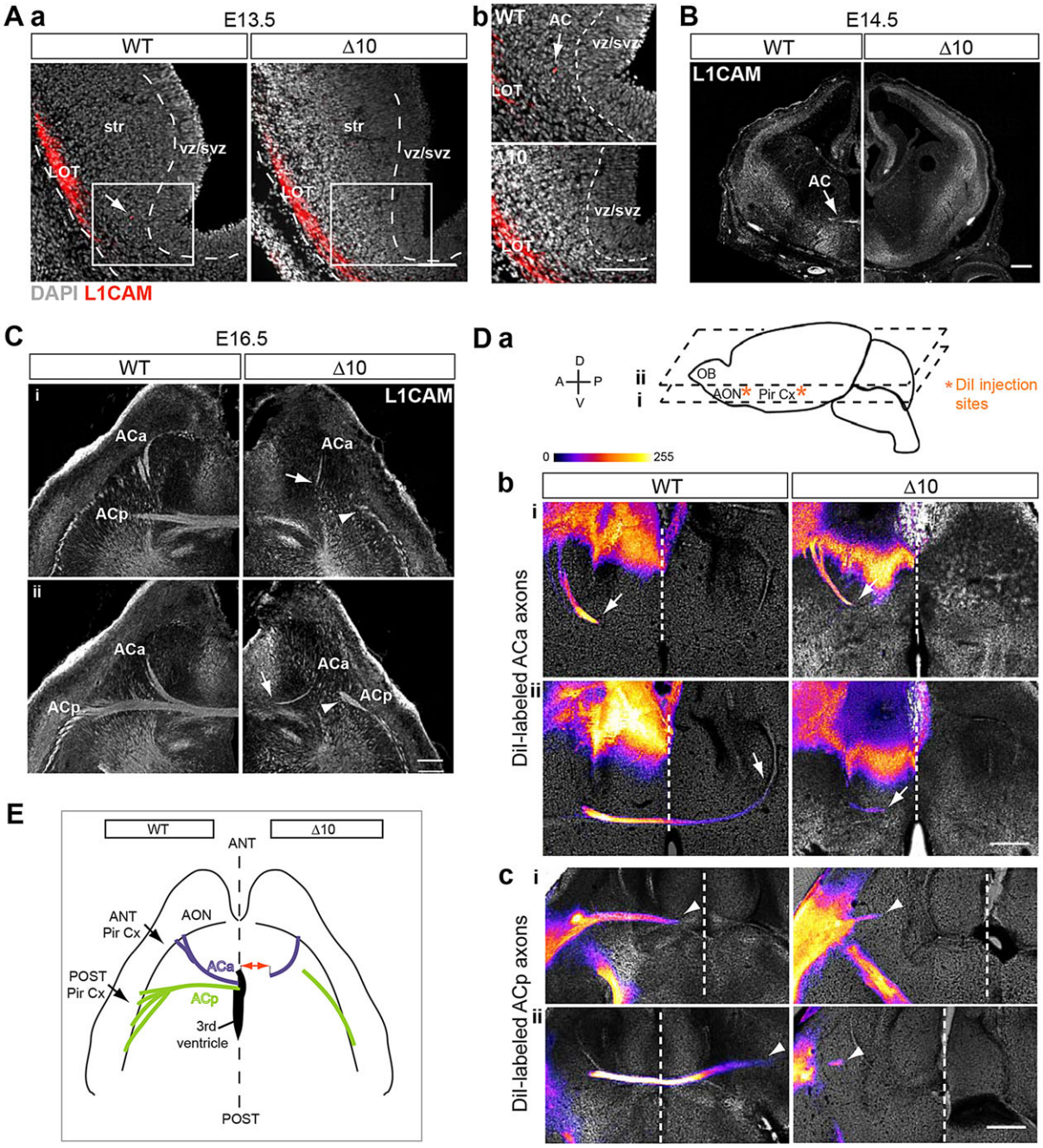

Fig. 2. *Schip1*Δ10 embryos display early defects in the development of the AC. AC morphological analyses were performed at E13.5, E14.5 and E16.5. (A) E13.5 coronal brain sections immunolabeled for L1CAM (red) and stained with DAPI (gray). (Ab) Higher magnification of boxed areas in Aa. Arrow, AC axons detected in WT; dashed lines, boundaries between the lateral olfactory tract (LOT), the striatum (str) and the ventricular/subventricular zones (vz/svz). (B) E14.5 coronal brain sections immunolabeled for L1CAM. Arrow, AC axons at the midline in WT. (C) E16.5 serial horizontal brain sections immunolabeled for L1CAM. Arrows, ACa in Δ10; arrowheads, ACp in Δ10. (D) DiI injection in E16.5 fixed brains. (Da) Schematic representation of DiI injection sites (asterisks) in the anterior piriform cortex (Pir Cx)/AON to label ACa axons (Db) and in the posterior piriform cortex to label ACp axons (Dc). Dashed lines, levels of the two serial horizontal sections (i,ii) presented in C and D. (Db,Dc) Phase-contrast images presented with pseudocolored DiI labeling. Dashed lines, brain midline; arrows, ACa; arrowheads, ACp. (E) Schematic representation of AC defects in Δ10 brains as compared with WT brains at E16.5. Red arrow, measured distance between ACa axons and the midline. Images are representative of *n*=4 (A-C) or *n*=3 (D) animals/genotype. Scale bars: 250 µm in A; 400 µm in B; 500 µm in C,D.

within layer 2, the most affected layer in Δ10 mutant mice (supplementary material Fig. S4A, high magnification panel). RT-PCR also revealed the expression of *Schip1* isoforms (mainly SCHIP1b, SCHIP1c and IQCJs-SCHIP1) in WT E14.5 piriform cortex (supplementary material Fig. S4C). *Schip1* expression appeared to be higher in the anterior piriform cortex than in the posterior piriform cortex (supplementary material Fig. S4B,D).

The early expression of *Schip1* prompted us to further characterize SCHIP1 functions during axon formation in piriform cortex neurons using *in vitro* approaches. Cultures were performed from E14.5 embryos, a stage of active axon growth in WT embryos and at which the thickness of the cortex is unaffected in mutants (Fig. 3B). We first estimated axon growth by quantifying the surface covered by the axons of anterior and posterior piriform cortex

Development (2015) 142, 2026-2036 doi:10.1242/dev.119248

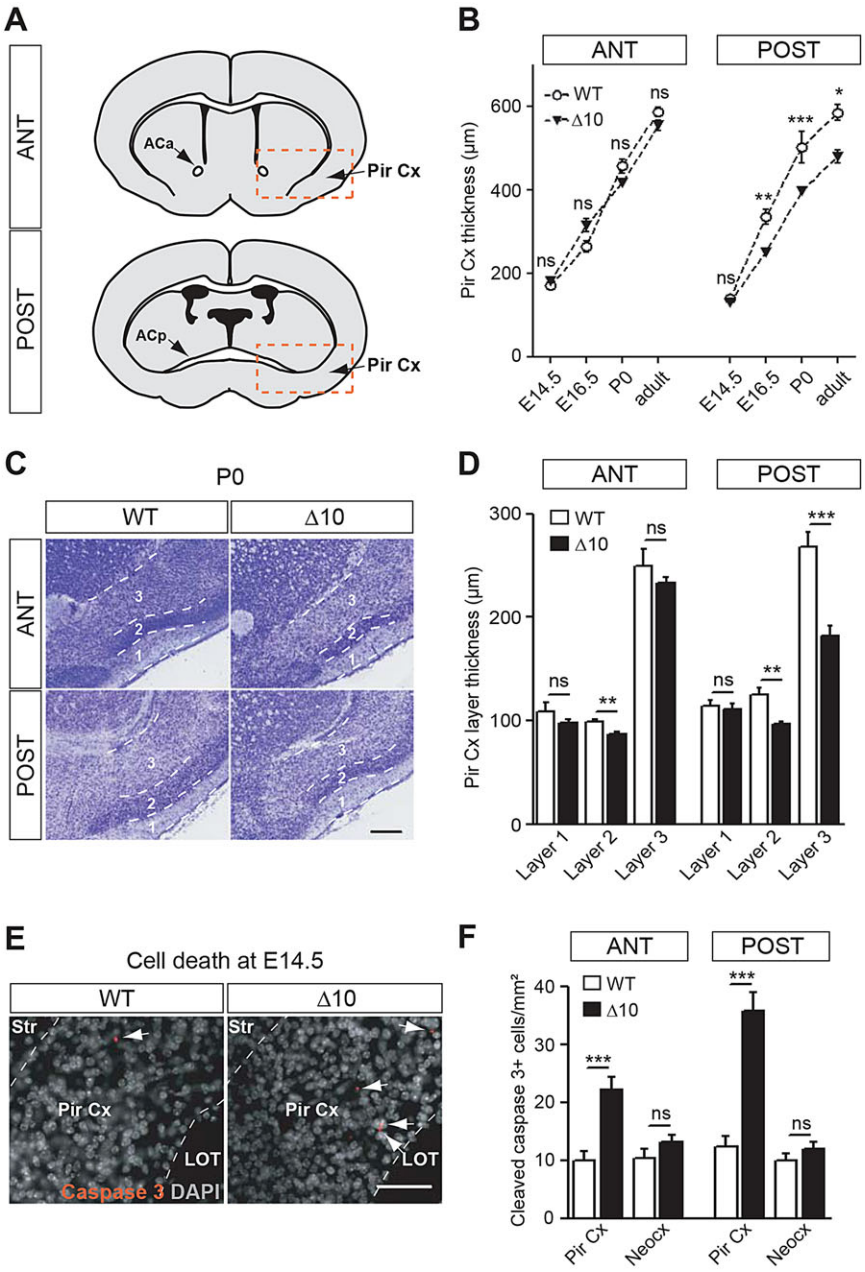

Fig. 3. *Schip1*Δ10 mice display thinner piriform cortex layers of projection neurons from E16.5, with increased cell death at E14.5. (A) Schematic representations of coronal brain sections used for piriform cortex (Pir Cx) analyses at the level of the ACa, as termed the anterior (ANT) region, and at the level of the ACp, as termed the posterior (POST) region. Red boxes indicate regions used for morphological analyses. (B) Piriform cortex thickness during development measured on Cresyl Violet-stained sections. (C) Cresyl Violet staining of P0 coronal sections. Dashed lines indicate boundaries of layers 1-3. (D) Thickness of piriform cortex layers at P0 measured on Cresyl Violet-stained sections as in C. (E) E14.5 coronal sections of posterior piriform cortex immunolabeled for cleaved caspase 3 (red) and stained with DAPI (gray). Arrows, cleaved caspase 3-positive cells. (F) Quantification of cleaved caspase 3-positive cell density at E14.5 in piriform cortex and neocortex (Neocx). Data are mean± s.e.m. *n*=3-5 animals/genotype/age, *n*=3 sections/animal (B); *n*=5 animals/genotype, *n*=3 sections/animal (C,D); *n*=3 animals/genotype, *n*=3 sections/animal (E,F). Two-way ANOVA (B,F), *t*-test (D); **P*<0.05, ***P*<0.01, ****P*<0.001; ns, not significant. Scale bars: 200 μm in C; 50 μm in E.

explants immunolabeled for TUJ1 (TUBB3) after 2 days in culture (Fig. 4A). Axon growth areas of mutant explants were significantly reduced compared with those of WT explants (Fig. 4B). Defects were similar for anterior and posterior piriform cortex explants.

To decipher which step of axon development was impaired by the Δ10 mutation, we cultured dissociated piriform cortex neurons. Characterization of these cultures indicated that neurons (TUJ1-immunopositive cells), which represented more than 80% of the total number of cells, started to develop by generating lamellipodia and later minor processes, and then formed one longer process (axon) within 2 days *in vitro* (DIV). In addition, 80% of neurons expressed the cell adhesion molecule NRCAM, which is known to be important during piriform cortex development (Lustig et al., 2001) (data not shown). RT-PCR confirmed that WT dissociated neurons expressed the same *Schip1* isoforms as those expressed in E14.5 piriform cortex *in vivo* (data not shown). No differences in neuronal density or percentage of cleaved caspase 3-immunopositive neurons were observed between WT and mutant cultures up to DIV4 or DIV6, respectively (supplementary material Table S4), demonstrating that, unlike *in vivo*, there was no obvious increase in cell death in cultures from mutant embryos.

We next analyzed neuronal morphology in these cultures. The immature neuritogenesis stage was over-represented in mutant cultures at DIV1 and DIV2 (Fig. 4C), suggesting a role for SCHIP1 in axon initiation. Measurements performed on neurons that exhibited one longer process and several shorter neurites (Fig. 4D) showed decreased axon length in mutant neurons at DIV1, DIV2 (Fig. 4D,E) and DIV4 (data not shown). This defect was rescued by expression of the Flag-tagged SCHIP1b isoform in mutant neurons (Fig. 4F,G). These data indicated a role for SCHIP1 in axon elongation, which was consistent with the distribution of SCHIP1 within growing neurons. Flag-tagged SCHIP1b indeed displayed a punctate localization along the neurites and in the growth cones, where it was found in the central region but also in the peripheral F-actin-rich domains that drive axon

Development (2015) 142, 2026-2036 doi:10.1242/dev.119248

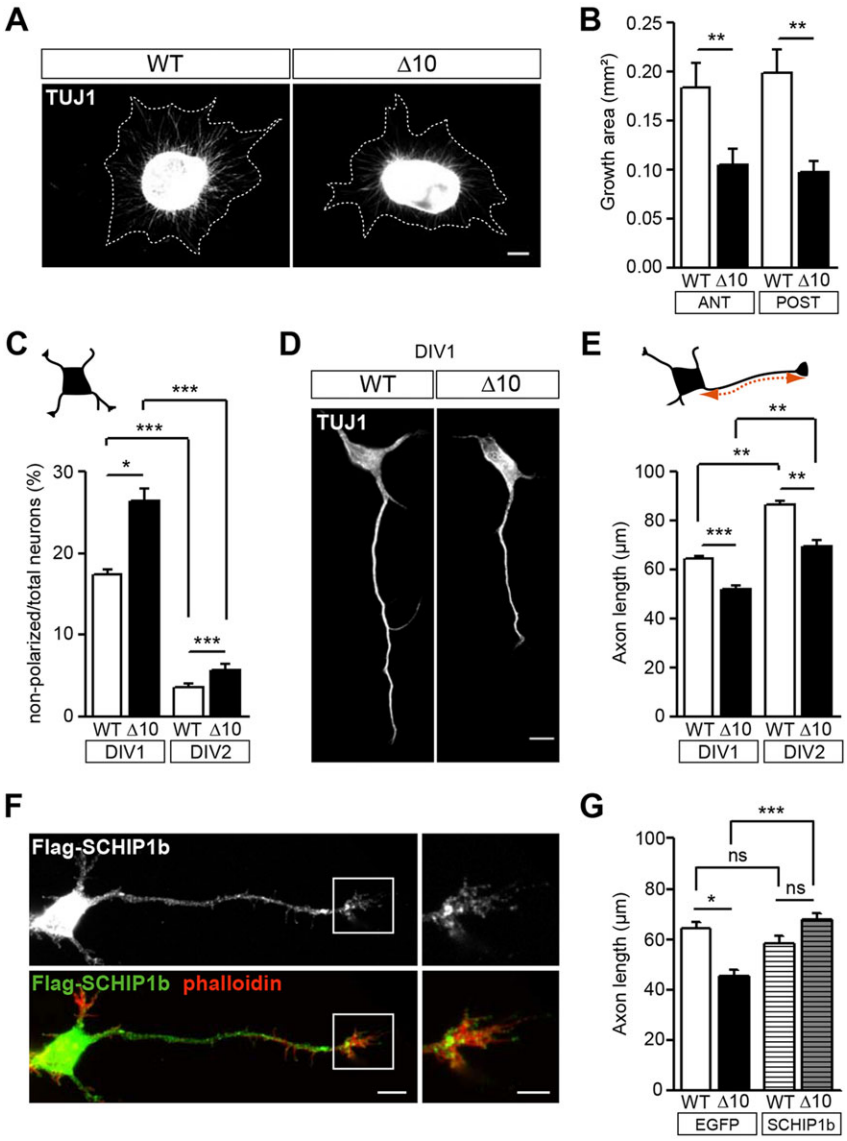

Fig. 4. SCHIP1 plays a role in axon initiation and outgrowth. (A,B) Axon growth analysis of E14.5 anterior and posterior piriform cortex explants in culture. (A) Posterior cortical explants immunolabeled for β3-tubulin (TUJ1). Dotted lines delineate the axon growth area. (B) Axon growth area quantification. (C-E) Morphological analyses of E14.5 piriform cortex dissociated neurons immunolabeled for TUJ1 after 1 or 2 days in culture (DIV). (C) Percentage of non-polarized neurons. (D) Axon length measurements in neurons that elongated an axon at DIV1. (E) Quantification of axon lengths at DIV1 and DIV2. (F,G) Rescue of axon outgrowth by expression of Flag-tagged SCHIP1b in E14.5 piriform cortex dissociated neurons. Axon length measurements in neurons expressing EGFP alone or EGFP and Flag-SCHIP1b at DIV2. (F) Representative mutant neuron expressing Flag-tagged SCHIP1b immunolabeled with anti-Flag antibody (green) and stained with phalloidin (red). The boxed regions showing the growth cone are magnified to the right. (G) Quantification of axon lengths at DIV2. Data are mean±s.e.m. *n*=8-10 embryos/genotype, *n*=6 explants/embryo (A,B); *n*=3 (DIV1)-10 (DIV2) embryos/genotype, *n*=100 neurons/embryo (C,E); *n*=3-5 embryos/genotype, *n*=40 neurons/embryo (G). Mann–Whitney; **P*<0.05, ***P*<0.01, ****P*<0.001; ns, not significant. Scale bars: 200 µm in A; 10 µm in D,F (low magnification); 5 µm in F (high magnification).

elongation (lamellipodia and filopodia) (Fig. 4F). The same localization was observed for SCHIP1c and IQCJs-SCHIP1 isoforms (data not shown).

SCHIP1 participates in posterior piriform cortex axon guidance and is implicated in the response to SEMA3F

Our results suggested that AC axons from mutant embryos might be misguided. Therefore, we asked how they respond to guidance cues from surrounding tissues. The lateral striatum is the first structure encountered by piriform cortex axons when they approach the midline and is known to express several guidance cues that control AC formation (Falk et al., 2005; Ho et al., 2009; Sahay et al., 2003). We analyzed the response of axons from E14.5 anterior and posterior piriform cortex explants to molecules secreted by lateral striatum explants in co-culture assays. Cortical explants, but not striatal explants, developed long axons within 24 h (Fig. 5A). We blindly determined a guidance index for cortical explants, as described previously (Castellani et al., 2000; Falk et al., 2005), which takes into account the density and the length of axons growing towards and away from the striatal explant (Fig. 5A). We analyzed the response of piriform cortex axons to striatal explants from embryos of either the same genotype or the 'opposite' genotype. In WT co-cultures, axons of anterior cortical explants were repelled by the striatum, whereas the axons of posterior cortical explants appeared unaffected, revealing specific and differential intrinsic guidance properties of the anterior and the posterior piriform cortices (Fig. 5B). The differential response of WT anterior and posterior piriform cortex axons was similar when co-cultured with Δ10 mutant striatum (Fig. 5B). The repulsive response of mutant anterior piriform cortex axons to the striatum was unaffected (Fig. 5B). By contrast, mutant posterior piriform cortex axons displayed significant repulsive responses when co-cultured with either WT or mutant striatum (Fig. 5B). Thus, the guidance properties of WT and mutant striatum appeared to be similar, suggesting that SCHIP1 does not play a key role in guidance molecule expression/secretion by the striatum. Accordingly, the expression patterns of the striatum-expressed guidance cue SEMA3F (Falk et al., 2005; Sahay et al., 2003) were similar in mutant and WT embryos (supplementary material Fig. S5). Overall, this suggested that SCHIP1 has an intrinsic function in the guidance mechanisms of ACp axons, allowing them to project toward the striatum.

Development (2015) 142, 2026-2036 doi:10.1242/dev.119248

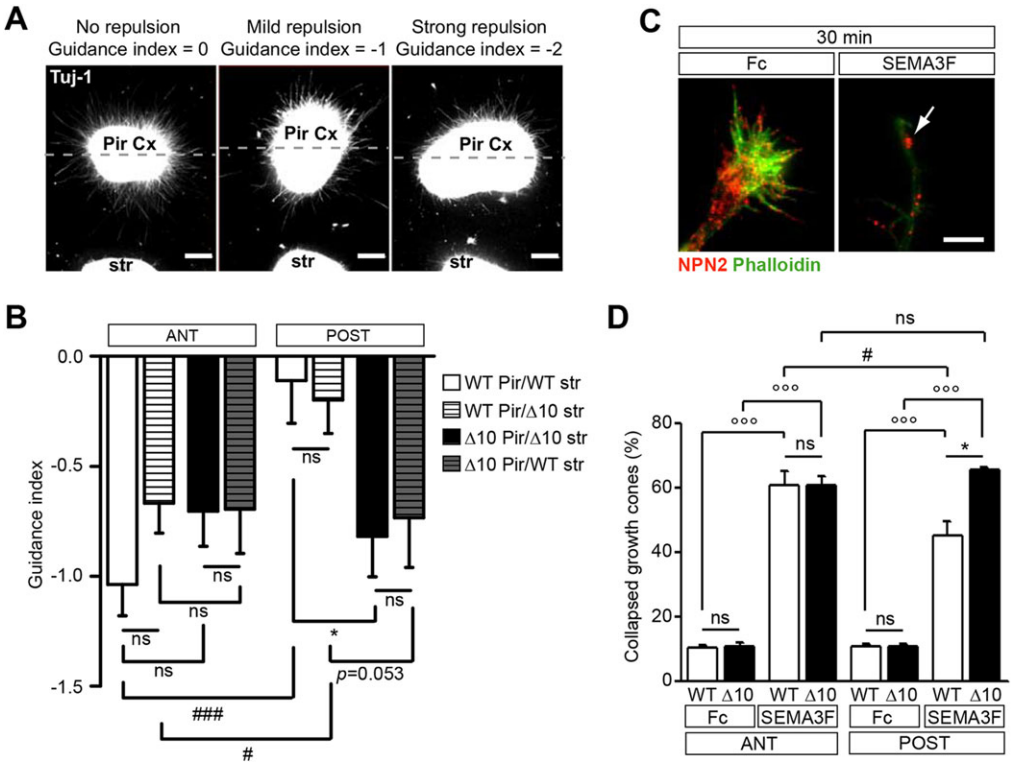

Fig. 5. SCHIP1 participates in posterior piriform cortex axon guidance and is implicated in the response to SEMA3F. (A,B) Co-cultures of explants from the anterior (ANT) or the posterior (POST) piriform cortex (Pir Cx) with lateral striatum explants (str) at E14.5. (A) Qualitative evaluation of guidance index based on the density and the length of axons growing toward or away from the lateral striatum explant. (B) Quantification of the guidance responses of piriform cortex (Pir) explants. (C,D) Cultures of dissociated neurons from ANT and POST piriform cortex incubated with 250 ng/ml Fc or SEMA3F-Fc (SEMA3F) for 30 min. (C) Growth cones immunolabeled for NPN2 (red) and stained with phalloidin (green) after Fc or SEMA3F treatment. Arrow, SEMA3F-induced collapse. (D) Percentage of collapsed growth cones. Data are mean±s.e.m. *n*=6-10 embryos/genotype, *n*=6 explants/embryo (B); *n*=5 embryos/genotype, *n*=50 growth cones/embryo (D). Mann-Whitney; *difference between genotypes;#difference between ANT and POST piriform cortex; °difference between treatments; $^{*/\#}P<0.05$; $^{\circ\circ\circ/\#\#\#}P<0.01$; ns, not significant. Scale bars: 200 µm in A; 5 µm in C.

SEMA3F plays a key role in AC formation through repulsive activity mediated by its interaction with the receptor neuropilin 2 (NPN2, or NRP2) expressed in the piriform cortex (Chen et al., 2000; Giger et al., 2000; Sahay et al., 2003). Mice mutant for *Sema3f* or *Npn2* display agenesis of the ACp, resembling the phenotype of Δ10 mice (Giger et al., 2000; Sahay et al., 2003). The expression pattern of *Npn2* was similar in E14.5 WT and Δ10 embryos (supplementary material Fig. S5). We therefore asked whether SCHIP1 could be directly implicated in the response of piriform cortex axons to SEMA3F. We performed collapse assays on dissociated anterior and posterior piriform cortex neurons separately by adding Fc-coupled SEMA3F (SEMA3F-Fc) or the Fc fragment alone to the culture medium. In control conditions, the proportion of collapsed growth cones immunolabeled for NPN2 (Fig. 5C) was low and similar in WT and mutant cultures, showing that the Δ10 mutation did not affect the basal rate of collapse (Fig. 5D). SEMA3F induced a collapse response of growth cones from both anterior and posterior piriform cortex neurons (Fig. 5C,D). Interestingly, the percentage of collapsed growth cones was 15.8% higher in anterior compared with posterior piriform cortex cultures (Fig. 5D). This indicated that, at E14.5, anterior piriform cortex neurons were more sensitive to SEMA3F than posterior piriform cortex neurons. The response of mutant anterior piriform cortex neurons to SEMA3F was similar to that of WT neurons (Fig. 5D). Intriguingly, mutant posterior piriform cortex cultures showed a 20.5% increase in the collapse response to SEMA3F as compared with WT cultures (Fig. 5D), indicating that SCHIP1 influences the response of posterior piriform cortex to SEMA3F. These results underscore the increased repulsion observed for mutant piriform cortex explants co-cultured with striatum (Fig. 5B), although axon guidance in explants undoubtedly results from a combination of responses to several guidance cues.

SCHIP1 participates in growth cone recovery after EPHB2-induced collapse

Non-secreted guidance molecules also control AC development, including EPHB2 and EPHA4 (Henkemeyer et al., 1996; Ho et al., 2009). Mice mutant for *Ephb2* present severe ACp defects, which resemble those of Δ10 mice. ACp defects are different in *Epha4* mutant mice, since ∼50% of ACp axons are misdirected into the ACa tract while the remainder exit the midline and resume projection to the contralateral hemisphere. We therefore chose to further address the potential role of SCHIP1 in response to the EPHB2 guidance cue. The interaction of EPHB2 with ephrin B2 expressed by AC axons is necessary for the proper guidance of ACp axons, notably in overriding repulsion mechanisms (Cowan et al., 2004). The extracellular domain of EPHB2 is sufficient to induce the collapse of growth cones expressing ephrin B (Mann et al., 2003).

In situ hybridizations showed that the expression patterns of EPHB2 were similar in E14.5 WT and Δ10 embryos (supplementary material Fig. S5). This prompted us to evaluate whether SCHIP1 could also be implicated in the response of axons to EPHB2 by adding the Fc-coupled extracellular domain of EPHB2 (EPHB2-Fc) to the culture medium. Immunolabeling for human Fc

Development (2015) 142, 2026-2036 doi:10.1242/dev.119248

after cell fixation confirmed that EPHB2-Fc bound to piriform cortex neurons (Fig. 6A). EPHB2-Fc induced the collapse of growth cones after 10 min in WT and mutant cultures (Fig. 6B,C). However, after 30 min, the number of collapsed growth cones was reduced in WT, whereas it remained high in mutant cultures (Fig. 6C). This effect was also observed in anterior and posterior piriform cortex cultures performed separately (data not shown). It was abolished by expression of the Flag-tagged SCHIP1b isoform in mutant neurons (Fig. 6D). In addition, the number of membrane-associated EPHB2-Fc puncta was higher in mutant than in WT collapsed growth cones after 30 min of EPHB2-Fc incubation, whereas it was similar after 10 min of incubation (Fig. 6E). These observations suggested that SCHIP1 influences growth cone recovery after EPHB2-induced collapse, possibly by controlling ephrin B levels at the membrane.

We further investigated this phenomenon by performing time-lapse imaging of growth cones (Fig. 6F,G). The onset of growth cone collapse was comparable in WT and mutant neurons (Fig. 6F). At 10 min of EPHB2-Fc incubation, the proportion of collapsed growth cones was similar in WT and mutant cultures. This proportion decreased in WT at 15 min of EPHB2-Fc incubation, whereas it remained unchanged in mutant cultures (Fig. 6G). These observations confirmed that SCHIP1 also controls the response of growth cones to EPHB2, allowing them to quickly recover after collapse.

DISCUSSION

In the present study, we demonstrate that the cytoskeleton-associated protein SCHIP1 plays an important role during brain development. We generated Δ10 mutant mice deficient for expression of all *Schip1*

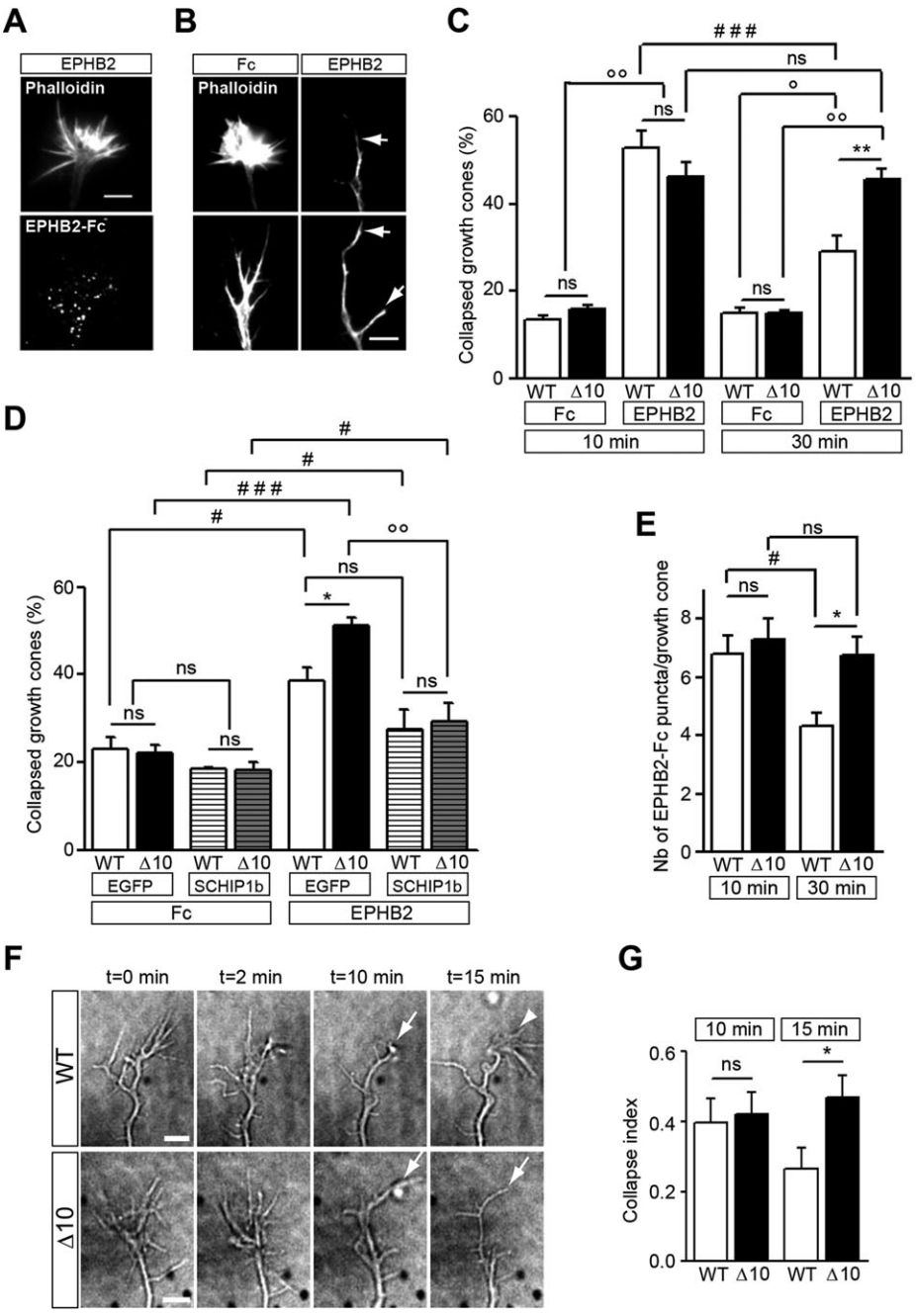

Fig. 6. SCHIP1 contributes to growth cone recovery after EPHB2-induced collapse. (A) Membrane-bound EPHB2-Fc (lower panel) detected by immunolabeling with an anti-Fc antibody on non-permeabilized fixed piriform cortex neurons. The dashed line on the lower panel delimits phalloidin staining, as shown on the upper panel. (B) Morphology of different growth cones of fixed piriform cortex neurons after Fc (left) or EPHB2-Fc (right) treatment for 10 min, as detected by phalloidin staining. Arrows, major filopodia of collapsed growth cones. (C) Percentage of collapsed growth cones after 10 or 30 min incubation with Fc or EPHB2-Fc (EPHB2). (D) Rescue of collapse response by expression of Flag-tagged SCHIP1b in neurons. The percentage of collapsed growth cones of neurons expressing either EGFP alone or EGFP and Flag-SCHIP1b (SCHIP1b) after 30 min incubation with Fc or EPHB2-Fc (EPHB2). (E) Quantification of the number of membrane EPHB2-Fc puncta per growth cone. (F) Time-lapse imaging of growth cone dynamics upon EPHB2-Fc treatment for 15 min. Arrows, collapse response; arrowhead, recovery response. (G) Proportion of collapsed growth cones after 10 or 15 min incubation with EPHB2-Fc. Data are mean±s.e.m. *n*=6 embryos/genotype, *n*=50 growth cones/embryo (C-E); *n*=3-6 embryos/genotype, *n*=20 growth cones/embryo (D); *n*=6 embryos/genotype, *n*=12 growth cones/embryo (G). Mann–Whitney (C-E), χ^2 (G); *, difference between genotypes; °, difference between treatments; #, difference between incubation times (C) or between Flag-SCHIP1b-expressing and non-expressing neurons (D); $^{*/\circ/\#}P<0.05$, $^{**/\circ\circ}P<0.01$, $^{\#\#\#}P<0.001$; ns, not significant. Scale bars: 5 µm.

Development (2015) 142, 2026-2036 doi:10.1242/dev.119248

isoforms and showed that they present a thinner piriform cortex and severe AC defects, which are likely to result from impaired axon growth and navigation. *In vitro* assays indicated that SCHIP1 modulates axon outgrowth and responses of growth cones to repulsive guidance cues in piriform cortex neurons. Remarkably, *Schip1*$^{Gt(ROSA)77Sor}$ mice, which lack expression of the SCHIP1a and IQCJ-SCHIP1 isoforms only (Chen et al., 2004), do not present AC defects (supplementary material Fig. S6). This supports the importance of SCHIP1b, SCHIP1c and IQCJs-SCHIP1, which are the most highly expressed isoforms during piriform cortex development, in AC formation.

In Δ10 mice, ACa and ACp display different morphological abnormalities: the ACa is present but thinner than in WT mice, whereas the ACp is absent. Developmental studies suggest that both ACa and ACp abnormalities result from a combination of altered axon outgrowth and guidance errors. *In vitro* studies of piriform cortex neurons support this hypothesis. Neurons from anterior and posterior mutant piriform cortex display impaired axon elongation without cell death and an impaired response to guidance cues required for AC formation. Expression analyses indicate that the different phenotypic severities of AC branches are not directly linked to the expression levels of *Schip1* in piriform cortex, but might be due to specific and differential intrinsic properties of the anterior and the posterior piriform cortex neurons. Consistently, we show that WT anterior piriform cortex axons are repelled by the striatum, whereas posterior piriform cortex axons are not. In addition, anterior piriform cortex neurons from WT E14.5 embryos display a higher sensitivity to SEMA3F than posterior piriform cortex neurons. Interestingly, the Δ10 mutation triggers the repulsion of posterior piriform cortex axons by the striatum, and enhances the response of posterior piriform cortex growth cones to SEMA3F. These results highlight specific guidance properties for posterior piriform cortex axons. Growth cone recovery after EPHB2-induced collapse also appears delayed in mutant axons. This indicates that SCHIP1 is required for the posterior piriform cortex axon response to at least two guidance cues, and further suggests that ACp agenesis in Δ10 mutants might result from impaired responses to these molecules, in combination with axon outgrowth defects.

Of note is the fact that Δ10 mutants represent the first mouse model with ACp agenesis associated with an increased axon sensitivity to repulsive guidance cues. So far, ACp agenesis was observed in mutant mice lacking guidance molecules, including SEMA3F, EPHB2, and their receptors NPN2 and ephrin B2, respectively. Thus, the similarity of ACp phenotypes in these mice and Δ10 mutants might appear counterintuitive. However, the developmental origins of the ACp agenesis in mice mutant for guidance molecules are likely to differ from that in Δ10 mutants. Indeed, in the absence of EPHB2, for instance, the ACp axons project aberrantly to the ventral forebrain (Henkemeyer et al., 1996; Ho et al., 2009), whereas this is not the case in Δ10 mutants. In mice deficient for axon guidance molecules, ACp agenesis may result from mistargeting of posterior piriform cortex axons to other brain regions followed by pruning. Changes in axon response to repulsive guidance cues in Δ10 mice could contribute to axon defects in different ways. The development of the axons requires adaptation mechanisms that allow their elongation toward a guidance cue gradient or the adjustment of their sensitivity to the environment (Ming et al., 2002; Piper et al., 2005). Growth cone recovery after collapse, which was observed by others (Campbell and Holt, 2001; Mann et al., 2003), could be one of these mechanisms, and the decrease of growth cone recovery seen in Δ10 mice could impair axon ability to navigate in a guidance cue gradient. In addition, the increased sensitivity of axons could induce axon degeneration and the death of the neurons, which normally project their axon through the AC. Indeed, both semaphorins and ephrins have been shown to promote cell death (Park et al., 2013; Vanderhaeghen and Cheng, 2010), and we observed cell death in E14.5 mutant piriform cortex, which is likely to depend on extrinsic factors since mutant neurons do not exhibit increased death *in vitro*. Alternatively, or in addition, mutant neurons impaired in axon growth might not reach anti-apoptotic factors, such as neurotrophic factors expressed at the midline (Barnes et al., 2007; Huang and Reichardt, 2001).

The exact mechanisms by which SCHIP1 controls axon development are unclear. Spontaneous neuronal activity was proposed to stimulate axon growth (Mire et al., 2012). The IQCJ-SCHIP1 isoform is a late component of the axon initial segment and could therefore play a role in controlling the excitability of mature neurons (Martin et al., 2008). However, this is unlikely to be the case in our *in vitro* experiments since we analyzed axon outgrowth at stages at which the axon initial segments have not yet formed (data not shown), hence suggesting earlier functions of SCHIP1 during axon development. Indeed, as an ankyrin-binding protein, SCHIP1 could participate in transmembrane protein localization and stabilization during early axon development. Axon outgrowth and guidance rely on a cascade of cellular events, including signal integration by CAMs and guidance receptors at the membrane and dynamic cytoskeletal reorganizations at the growth cones. L1-CAMs, which associate directly with ankyrins, have been implicated in multiple aspects of these processes (Gil et al., 2003; Herron et al., 2009; Kiryushko et al., 2004; Nishimura et al., 2003). Thus, SCHIP1 could mediate axon outgrowth by regulating ankyrin interactions and the responsiveness of L1-CAMs, such as L1CAM and NRCAM, expressed by piriform cortex neurons.

A role for SCHIP1 as an adaptor-associated protein within the cortical cytoskeleton would also be consistent with its involvement in the response of growth cones to repulsive cues. In the context of AC axons, the SEMA3F-activated signaling pathway involves the interaction of its receptor NPN2 with NRCAM (Falk et al., 2005). The interaction of NPN1 (NRP1) with L1CAM and TAG-1 (CNTN2) in response to SEMA3A induces endocytosis of the complex, which enhances the signaling pathway leading to repulsion (Castellani et al., 2000, 2004; Schmid et al., 2000). Similar mechanisms involving NRCAM could operate in AC axons in response to SEMA3F. Ankyrins have been suggested to control NRCAM dynamics at the membrane and L1CAM endocytosis (Falk et al., 2004; Needham et al., 2001). SCHIP1 could therefore participate in the SEMA3F-induced response by regulating ankyrin interactions with NRCAM and the stability of the NPN2-NRCAM complex at the membrane. In addition, ephrin B signal transduction upon EPHB-ephrin B interaction involves molecular pathways leading to repulsion (Xu and Henkemeyer, 2012). This process needs termination mechanisms, notably clathrin-mediated endocytosis of EPHB-ephrin B complexes, to lower receptor levels at the membrane and allow growth cone desensitization and adaptation to guidance cues (Georgakopoulos et al., 2006; Marston et al., 2003; Parker et al., 2004; Tomita et al., 2006; Zimmer et al., 2003). The persistence of high numbers of EPHB2-Fc clusters on the growth cone surface after long-lasting EPHB2-Fc incubation in mutant cultures suggests that SCHIP1 could contribute to the regulation of ephrin B internalization. It has been shown that L1CAM/CHL1 interacts with ephrin A and is required in repulsive responses (Demyanenko et al., 2011). Thus, SCHIP1 could be a component of ephrin-associated protein complexes containing L1-CAMs and ankyrins.

Development (2015) 142, 2026-2036 doi:10.1242/dev.119248

Beside ankyrins, SCHIP1 is able to associate with schwannomin, an actin-binding protein that links membrane proteins to the cortical cytoskeleton (McClatchey and Fehon, 2009). Schwannomin has been shown to play roles in axon growth and guidance (Lavado et al., 2014; Schulz et al., 2010; Yamauchi et al., 2008). However, whether schwannomin contributes to SCHIP1-mediated axon outgrowth and guidance is uncertain since SCHIP1 and schwannomin expression patterns are different during brain development (Huynh et al., 1996). In addition, *Nf2*$^{F/F}$*;Emx1-cre* mice do not present AC defects but instead CC agenesis, which does not result from a lack of schwannomin in callosal neurons or their progenitors but in midline neural progenitor cells (Lavado et al., 2014). Schwannomin appeared to regulate guidance cue expression, whereas SCHIP1 does not and is directly involved in axon development.

In conclusion, our study reveals a role for a cytoskeleton-associated protein in AC and, to a lesser extent, in CC axon development. It highlights that intracellular mechanisms, directly downstream of surface molecules, also need to be considered in axonal tract development. *Schip1*Δ10 mice potentially represent a unique model to better understand these mechanisms. In addition, these mice can be helpful in dissecting piriform cortex functions in olfaction since they display behavioral and cognitive deficits that might be related to piriform cortex dysfunction (our unpublished results).

MATERIALS AND METHODS

Antibodies

The description and characterization of SCHIP1 antibodies are presented in supplementary material Methods and Fig. S2; other antibodies are listed in supplementary material Table S5.

Schip1 mutant mice

The identification of mouse SCHIP1 isoforms, generation and characterization of *Schip1* mutant mice, and animal procedures (including ethics statement) are described in supplementary material Methods, Fig. S1 (*Schip1*Δ10 mice) and Fig. S6 [*Schip1*$^{Gt(ROSA)77Sor}$ mice].

Primary cultures of dissociated neurons and explants

Primary cultures of dissociated neurons were performed as described in supplementary material Methods. To express SCHIP1 isoforms in neurons, *Schip1* cDNAs were fused by PCR 3′ to nucleotides encoding the tag Flag and cloned into a pCIG plasmid (Megason and McMahon, 2002) that allows co-expression of EGFP in nuclei. Constructs were electroporated in neurons before plating using the Neon Transfection System (Invitrogen) according to the manufacturer's protocol (two 20-ms pulses, 1350 V). For collapse assays, SEMA3F-Fc (R&D Systems, #3237-S3-025), EPHB2-Fc (R&D Systems, #467-B2-200) and control Fc fragment (Rockland, #009-0103) were added to the culture medium 2 days after plating, at the lowest concentration at which a collapse response was observed (250 ng/ml). For explant cultures, pieces of tissue comprising the anterior piriform cortex and the AON or more posteriorly located piriform cortex were dissected from E14.5 embryos and manually cut into ∼500 µm diameter explants. For co-culture experiments, the lateral striatum lining the piriform cortex was dissected and cut into ∼700 µm diameter explants. Explant cultures were performed in three-dimensional plasma clots as described previously (Castellani et al., 2000) and fixed in 4% paraformaldehyde/10% sucrose/PBS after 24 h in culture.

Histological/cytological analyses

Tissue processing, immunostaining, immunoprecipitations from brain lysates, acetylcholinesterase and X-gal staining, Nissl coloration, BrdU injection and detection, axon visualization by fluorescent lipophilic tracers and *in situ* hybridization were performed using standard protocols as described in supplementary material Methods.

Image acquisitions and analyses

Images were acquired as described in supplementary material Methods and analyses were performed using ImageJ software (NIH). The thickness of the neocortex, the piriform cortex and its three layers was measured on coronal sections throughout the anteroposterior axis. Three sections were quantified and averaged per animal. Three equidistant lines perpendicular to the surface of the layers were drawn on each image as described previously (Sarma et al., 2011). The thickness of each layer was measured along these three lines and averaged per section. For morphological studies of dissociated neurons, the length of axons was measured using the NeuronJ plug-in. For explant axon growth experiments, the axon growth area was calculated by subtracting the explant area from the total area occupied by the explant and the axons. To estimate axon guidance we used a qualitative guidance index as described previously (Castellani et al., 2000; Falk et al., 2005). The global influence of the lateral striatum on the piriform cortex axon trajectories was scored blindly from −2 (when most axons grew away from the lateral striatum) to 2 (when most axons grew toward the lateral striatum).

To quantify the proportions of collapsed growth cones, we defined as control growth cones those that exhibited complex profiles with multiple filopodia and broad lamellipodia, and as collapsed growth cones those that typically lacked lamellipodia and possessed only one or two major F-actin-positive filopodia. For time-lapse experiments, phase-contrast imaging revealed very small protrusions (<2 µm) in addition to major filopodia in certain collapsing growth cones, which were not detectable by phalloidin staining on fixed neurons and that were assumed to correspond to retracting filopodia undergoing actin depolymerization. They were not considered as 'major' filopodia. For quantification, a value of 1 was assigned to collapsed growth cones and a value of 0 to non-collapsed growth cones. The proportion was defined as the number of values 1 compared with the total number of values. Statistical analyses were performed as described in supplementary material Methods.

Acknowledgements

We are grateful to R. Boukhari, A. Rousseau, S. Thomasseau and M. Savariradjane (Institut du Fer à Moulin) for animal care, genotyping and assistance with microscopy; D. Godefroy (Institut de la Vision imaging platform) for technical support with nanozoomer acquisitions; A. Bellon (Development and Neuroscience Department, Cambridge University) for advice on piriform cortex cultures; and M. Nosten-Bertrand, F. Francis, P. Gaspar and R. Belvindrah (Institut du Fer à Moulin) for help with statistical analyses and critically reading the manuscript.

Competing interests

The authors declare no competing or financial interests.

Author contributions

Project design: E.K., P.-M.M., J.-A.G., J.F., A.C. and L.G. Molecular biology and biochemical experiments: E.K., P.-M.M. and L.G. Δ10 mouse generation: P.-M.M., F.C. and M.Gi. Histological and culture experiments: E.K., M.Ga., C.M.-F. and L.G. Manuscript writing: E.K., J.F., A.C., J.-A.G. and L.G.

Funding

This work was supported by Inserm, Université Pierre et Marie Curie, and grants from the Fondation Orange [14/2009], the Fondation de France [2009006047], the Fondation pour la Recherche Médicale (FRM) [FDT20130928180] and the Région Ile de France (NERF) [10016908] to the Institut du Fer à Moulin for common facilities. E.K. was the recipient of a doctoral fellowship from the Ministère de la Recherche et de l'Enseignement Supérieur. The teams of J.-A.G., A.C. and L.G. are affiliated with the Paris School of Neuroscience (ENP). The teams of J.-A.G. and L.G. are affiliated with the Bio-Psy Laboratory of Excellence.

Supplementary material

Supplementary material available online at
http://dev.biologists.org/lookup/suppl/doi:10.1242/dev.119248/-/DC1

References

Barnes, A. P., Lilley, B. N., Pan, Y. A., Plummer, L. J., Powell, A. W., Raines, A. N., Sanes, J. R. and Polleux, F. (2007). LKB1 and SAD kinases define a pathway required for the polarization of cortical neurons. *Cell* **129**, 549-563.

Bekkers, J. M. and Suzuki, N. (2013). Neurons and circuits for odor processing in the piriform cortex. *Trends Neurosci.* **36**, 429-438.

Bennett, V. and Lorenzo, D. N. (2013). Spectrin- and ankyrin-based membrane domains and the evolution of vertebrates. *Curr. Top. Membr.* **72**, 1-37.

Buttermore, E. D., Thaxton, C. L. and Bhat, M. A. (2013). Organization and maintenance of molecular domains in myelinated axons. *J. Neurosci. Res.* **91**, 603-622.
Campbell, D. S. and Holt, C. E. (2001). Chemotropic responses of retinal growth cones mediated by rapid local protein synthesis and degradation. *Neuron* **32**, 1013-1026.
Castellani, V., Chédotal, A., Schachner, M., Faivre-Sarrailh, C. and Rougon, G. (2000). Analysis of the L1-deficient mouse phenotype reveals cross-talk between Sema3A and L1 signaling pathways in axonal guidance. *Neuron* **27**, 237-249.
Castellani, V., Falk, J. and Rougon, G. (2004). Semaphorin3A-induced receptor endocytosis during axon guidance responses is mediated by L1 CAM. *Mol. Cell. Neurosci.* **26**, 89-100.
Chen, H., Bagri, A., Zupicich, J. A., Zou, Y., Stoeckli, E., Pleasure, S. J., Lowenstein, D. H., Skarnes, W. C., Chédotal, A. and Tessier-Lavigne, M. (2000). Neuropilin-2 regulates the development of selective cranial and sensory nerves and hippocampal mossy fiber projections. *Neuron* **25**, 43-56.
Chen, W. V., Delrow, J., Corrin, P. D., Frazier, J. P. and Soriano, P. (2004). Identification and validation of PDGF transcriptional targets by microarray-coupled gene-trap mutagenesis. *Nat. Genet.* **36**, 304-312.
Colavita, A. and Culotti, J. G. (1998). Suppressors of ectopic UNC-5 growth cone steering identify eight genes involved in axon guidance in Caenorhabditis elegans. *Dev. Biol.* **194**, 72-85.
Cowan, C. A., Yokoyama, N., Saxena, A., Chumley, M. J., Silvany, R. E., Baker, L. A., Srivastava, D. and Henkemeyer, M. (2004). Ephrin-B2 reverse signaling is required for axon pathfinding and cardiac valve formation but not early vascular development. *Dev. Biol.* **271**, 263-271.
Cummings, D. M., Malun, D. and Brunjes, P. C. (1997). Development of the anterior commissure in the opossum: midline extracellular space and glia coincide with early axon decussation. *J. Neurobiol.* **32**, 403-414.
de Castro, F. (2009). Wiring olfaction: the cellular and molecular mechanisms that guide the development of synaptic connections from the nose to the cortex. *Front. Neurosci.* **3**, 52.
Demyanenko, G. P., Siesser, P. F., Wright, A. G., Brennaman, L. H., Bartsch, U., Schachner, M. and Maness, P. F. (2011). L1 and CHL1 cooperate in thalamocortical axon targeting. *Cereb. Cortex* **21**, 401-412.
Falk, J., Thoumine, O., Dequidt, C., Choquet, D. and Faivre-Sarrailh, C. (2004). NrCAM coupling to the cytoskeleton depends on multiple protein domains and partitioning into lipid rafts. *Mol. Biol. Cell* **15**, 4695-4709.
Falk, J., Bechara, A., Fiore, R., Nawabi, H., Zhou, H., Hoyo-Becerra, C., Bozon, M., Rougon, G., Grumet, M., Püschel, A. W. et al. (2005). Dual functional activity of semaphorin 3B is required for positioning the anterior commissure. *Neuron* **48**, 63-75.
Georgakopoulos, A., Litterst, C., Ghersi, E., Baki, L., Xu, C., Serban, G. and Robakis, N. K. (2006). Metalloproteinase/Presenilin1 processing of ephrinB regulates EphB-induced Src phosphorylation and signaling. *EMBO J.* **25**, 1242-1252.
Giger, R. J., Cloutier, J.-F., Sahay, A., Prinjha, R. K., Levengood, D. V., Moore, S. E., Pickering, S., Simmons, D., Rastan, S., Walsh, F. S. et al. (2000). Neuropilin-2 is required in vivo for selective axon guidance responses to secreted semaphorins. *Neuron* **25**, 29-41.
Gil, O. D., Sakurai, T., Bradley, A. E., Fink, M. Y., Cassella, M. R., Kuo, J. A. and Felsenfeld, D. P. (2003). Ankyrin binding mediates L1CAM interactions with static components of the cytoskeleton and inhibits retrograde movement of L1CAM on the cell surface. *J. Cell Biol.* **162**, 719-730.
Goutebroze, L., Brault, E., Muchardt, C., Camonis, J. and Thomas, G. (2000). Cloning and characterization of SCHIP-1, a novel protein interacting specifically with spliced isoforms and naturally occurring mutant NF2 proteins. *Mol. Cell. Biol.* **20**, 1699-1712.
Henkemeyer, M., Orioli, D., Henderson, J. T., Saxton, T. M., Roder, J., Pawson, T. and Klein, R. (1996). Nuk controls pathfinding of commissural axons in the mammalian central nervous system. *Cell* **86**, 35-46.
Herron, L. R., Hill, M., Davey, F. and Gunn-Moore, F. J. (2009). The intracellular interactions of the L1 family of cell adhesion molecules. *Biochem. J.* **419**, 519-531.
Ho, S. K. Y., Kovačević, N., Henkelman, R. M., Boyd, A., Pawson, T. and Henderson, J. T. (2009). EphB2 and EphA4 receptors regulate formation of the principal inter-hemispheric tracts of the mammalian forebrain. *Neuroscience* **160**, 784-795.
Huang, E. J. and Reichardt, L. F. (2001). Neurotrophins: roles in neuronal development and function. *Annu. Rev. Neurosci.* **24**, 677-736.
Huang, T.-N., Chuang, H.-C., Chou, W.-H., Chen, C.-Y., Wang, H.-F., Chou, S.-J. and Hsueh, Y.-P. (2014). Tbr1 haploinsufficiency impairs amygdalar axonal projections and results in cognitive abnormality. *Nat. Neurosci.* **17**, 240-247.
Huynh, D. P., Tran, T. M., Nechiporuk, T. and Pulst, S. M. (1996). Expression of neurofibromatosis 2 transcript and gene product during mouse fetal development. *Cell Growth Differ.* **7**, 1551-1561.
Kiryushko, D., Berezin, V. and Bock, E. (2004). Regulators of neurite outgrowth: role of cell adhesion molecules. *Ann. N. Y. Acad. Sci.* **1014**, 140-154.
Kunimoto, M. and Suzuki, T. (1995). Selective down-regulation of 440 kDa ankyrinB associated with neurite retraction. *Neuroreport* **6**, 2545-2548.
Lavado, A., Ware, M., Pare, J. and Cao, X. (2014). The tumor suppressor Nf2 regulates corpus callosum development by inhibiting the transcriptional coactivator Yap. *Development* **141**, 4182-4193.
Lindwall, C., Fothergill, T. and Richards, L. J. (2007). Commissure formation in the mammalian forebrain. *Curr. Opin. Neurobiol.* **17**, 3-14.
Lustig, M., Erskine, L., Mason, C. A., Grumet, M. and Sakurai, T. (2001). Nr-CAM expression in the developing mouse nervous system: ventral midline structures, specific fiber tracts, and neuropilar regions. *J. Comp. Neurol.* **434**, 13-28.
Mann, F., Miranda, E., Weinl, C., Harmer, E. and Holt, C. E. (2003). B-type Eph receptors and ephrins induce growth cone collapse through distinct intracellular pathways. *J. Neurobiol.* **57**, 323-336.
Marston, D. J., Dickinson, S. and Nobes, C. D. (2003). Rac-dependent trans-endocytosis of ephrinBs regulates Eph-ephrin contact repulsion. *Nat. Cell Biol.* **5**, 879-888.
Martin, P.-M., Carnaud, M., del Cano, G. G., Irondelle, M., Irinopoulou, T., Girault, J.-A., Dargent, B. and Goutebroze, L. (2008). Schwannomin-interacting protein-1 isoform IQCJ-SCHIP-1 is a late component of nodes of Ranvier and axon initial segments. *J. Neurosci.* **28**, 6111-6117.
McClatchey, A. I. and Fehon, R. G. (2009). Merlin and the ERM proteins–regulators of receptor distribution and signaling at the cell cortex. *Trends Cell Biol.* **19**, 198-206.
Megason, S. G. and McMahon, A. P. (2002). A mitogen gradient of dorsal midline Wnts organizes growth in the CNS. *Development* **129**, 2087-2098.
Ming, G.-L., Wong, S. T., Henley, J., Yuan, X.-B., Song, H.-J., Spitzer, N. C. and Poo, M.-M. (2002). Adaptation in the chemotactic guidance of nerve growth cones. *Nature* **417**, 411-418.
Mire, E., Mezzera, C., Leyva-Díaz, E., Paternain, A. V., Squarzoni, P., Bluy, L., Castillo-Paterna, M., López, M. J., Peregrín, S., Tessier-Lavigne, M. et al. (2012). Spontaneous activity regulates Robo1 transcription to mediate a switch in thalamocortical axon growth. *Nat. Neurosci.* **15**, 1134-1143.
Needham, L. K., Thelen, K. and Maness, P. F. (2001). Cytoplasmic domain mutations of the L1 cell adhesion molecule reduce L1-ankyrin interactions. *J. Neurosci.* **21**, 1490-1500.
Nishimura, K., Yoshihara, F., Tojima, T., Ooashi, N., Yoon, W., Mikoshiba, K., Bennett, V. and Kamiguchi, H. (2003). L1-dependent neuritogenesis involves ankyrinB that mediates L1-CAM coupling with retrograde actin flow. *J. Cell Biol.* **163**, 1077-1088.
Park, E., Kim, Y., Noh, H., Lee, H., Yoo, S. and Park, S. (2013). EphA/ephrin-A signaling is critically involved in region-specific apoptosis during early brain development. *Cell Death Differ.* **20**, 169-180.
Parker, M., Roberts, R., Enriquez, M., Zhao, X., Takahashi, T., Pat Cerretti, D., Daniel, T. and Chen, J. (2004). Reverse endocytosis of transmembrane ephrin-B ligands via a clathrin-mediated pathway. *Biochem. Biophys. Res. Commun.* **323**, 17-23.
Piper, M., Salih, S., Weinl, C., Holt, C. E. and Harris, W. A. (2005). Endocytosis-dependent desensitization and protein synthesis-dependent resensitization in retinal growth cone adaptation. *Nat. Neurosci.* **8**, 179-186.
Pires-Neto, M. A. and Lent, R. (1993). The prenatal development of the anterior commissure in hamsters: pioneer fibers lead the way. *Brain Res. Dev. Brain Res.* **72**, 59-66.
Sahay, A., Molliver, M. E., Ginty, D. D. and Kolodkin, A. L. (2003). Semaphorin 3F is critical for development of limbic system circuitry and is required in neurons for selective CNS axon guidance events. *J. Neurosci.* **23**, 6671-6680.
Sarma, A. A., Richard, M. B. and Greer, C. A. (2011). Developmental dynamics of piriform cortex. *Cereb. Cortex* **21**, 1231-1245.
Schmahl, J., Raymond, C. S. and Soriano, P. (2007). PDGF signaling specificity is mediated through multiple immediate early genes. *Nat. Genet.* **39**, 52-60.
Schmahl, J., Rizzolo, K. and Soriano, P. (2008). The PDGF signaling pathway controls multiple steroid-producing lineages. *Genes Dev.* **22**, 3255-3267.
Schmid, R. S., Pruitt, W. M. and Maness, P. F. (2000). A MAP kinase-signaling pathway mediates neurite outgrowth on L1 and requires Src-dependent endocytosis. *J. Neurosci.* **20**, 4177-4188.
Schneider, S., Gulacsi, A. and Hatten, M. E. (2011). Lrp12/Mig13a reveals changing patterns of preplate neuronal polarity during corticogenesis that are absent in reeler mutant mice. *Cereb. Cortex* **21**, 134-144.
Schulz, A., Geissler, K. J., Kumar, S., Leichsenring, G., Morrison, H. and Baader, S. L. (2010). Merlin inhibits neurite outgrowth in the CNS. *J. Neurosci.* **30**, 10177-10186.
Scotland, P., Zhou, D., Benveniste, H. and Bennett, V. (1998). Nervous system defects of AnkyrinB (-/-) mice suggest functional overlap between the cell adhesion molecule L1 and 440-kD AnkyrinB in premyelinated axons. *J. Cell Biol.* **143**, 1305-1315.
Tomita, T., Tanaka, S., Morohashi, Y. and Iwatsubo, T. (2006). Presenilin-dependent intramembrane cleavage of ephrin-B1. *Mol. Neurodegener.* **1**, 2.
Vanderhaeghen, P. and Cheng, H.-J. (2010). Guidance molecules in axon pruning and cell death. *Cold Spring Harb. Perspect. Biol.* **2**, a001859.
Xu, N.-J. and Henkemeyer, M. (2012). Ephrin reverse signaling in axon guidance and synaptogenesis. *Semin. Cell Dev. Biol.* **23**, 58-64.
Yamauchi, J., Miyamoto, Y., Kusakawa, S., Torii, T., Mizutani, R., Sanbe, A., Nakajima, H., Kiyokawa, N. and Tanoue, A. (2008). Neurofibromatosis 2 tumor suppressor, the gene induced by valproic acid, mediates neurite outgrowth through interaction with paxillin. *Exp. Cell Res.* **314**, 2279-2288.
Zimmer, M., Palmer, A., Köhler, J. and Klein, R. (2003). EphB-ephrinB bi-directional endocytosis terminates adhesion allowing contact mediated repulsion. *Nat. Cell Biol.* **5**, 869-878.

SUPPLEMENTARY MATERIAL AND METHODS

Antibodies

The antibody α17141 was obtained by immunizing rabbits with GST fused to amino acids 112 to 305 of the SCHIP1a isoform (amino acids 187 to 380 of the IQCJ-SCHIP1 isoform; supplementary material Fig. S2A) (Goutebroze et al., 2000). The antibody α16280 was obtained by immunizing rabbits with GST fused to the amino acids encoded by *Schip1* exon 6 (amino acids 98 to 325 of IQCJ-SCHIP1; supplementary material Fig. S2A). The antibody HPA was from Sigma (#HPA003445) and was obtained by immunizing rabbits with a region of SCHIP1a encompassing amino-acids 47 to 165 (amino acids 122 to 240 of IQCJ-SCHIP1; supplementary material Fig. S2A). The antibody α959 was obtained by immunizing chickens with GST fused to a protein encompassing the last C-terminal 179 amino acids of SCHIP1 common to all isoforms (amino acids 381 to 559 of IQCJ-SCHIP1: supplementary material Fig. S2A) (Goutebroze et al., 2000). These antibodies where characterized by immunoblotting on lysates from COS-7 cells transfected with expressing vectors for Flag-tagged SCHIP1 isoforms (pFLAG-CMV-2 vector, Sigma-Aldrich) or Flag-tagged IQCJ-SCHIP1 truncated proteins corresponding to the cDNA of IQCJ-SCHIP1 deleted of exon 10, exons 10 and 11, or exons 10 to 12. The antibodies α17141, α16280 and αHPA recognized specifically the SCHIP1a and IQCJ-SCHIP1 isoforms, but not the four other SCHIP1 isoforms, indicating that the immunoglobulins are directed against the region encoded by *Schip1* exon 6, which is not present in the four other SCHIP1 isoforms (supplementary material Fig. S2B). They also recognized IQCJ-SCHIP1 truncated proteins (supplementary material Fig. S2C). The antibody α959 recognized all SCHIP1 isoforms but not truncated proteins (supplementary material Fig. S2B,C).

Identification of mouse SCHIP1 isoforms, and isoform mRNA expression analysis

The sequences coding for the mouse SCHIP1 isoforms SCHIP1a, SCHIP1b and IQCJ-SCHIP1, were previously identified (Martin et al., 2008) (GenBank accession numbers: SCHIP1a, EU163407; SCHIP1b, EU163408; IQCJs-SCHIP1, EU163409). The sequences coding for isoforms SCHIP1c, SCHIP1d and IQCJs-SCHIP1, were identified by screening the mouse genome and EST databases at NCBI using the basic local alignment search tool. The corresponding cDNAs were isolated by reverse transcription/amplification (RT/PCR) experiments from mouse brain mRNA and sequenced. The cDNA sequences were deposited in GenBank (accession numbers: SCHIP1c, KM233716; SCHIP1d, KM233715; IQCJs-SCHIP1, KJ941154). For isoform mRNA expression analysis, RT/PCR were performed using a common antisense primer (5'- CGGGACAGTAAGCTCGGACGTTAC) and the following isoform specific sense primers:

SCHIP1a (5'- GCAAGCTGACAGAGATTACCGAGAGG);

SCHIP1b (5'- GCAAGCTGACAGAGCACAGAAGAATGAG);

SCHIP1c (5'- TCAGGAGAACTGCTCGTACCAGG);

SCHIP1d (5'- GCAGTTGGCACTTCAGCCTGTCA);

IQCJ-SCHIP1 (5'- CAGCAGCACACCCGATTACCGAGAGG);

IQCJs-SCHIP1 (5'- CAGCAGCACACCCGCACAGAAGAATGAG).

The expected sizes of amplified DNA fragments were the following: SCHIP1a, 1549 bp; SCHIP1b, 853 bp; SCHIP1c, 865 bp; SCHIP1d, 939 bp; IQCJ-SCHIP1, 1537 bp; IQCJs-SCHIP1, 853 bp.

For expression analysis of the housekeeping gene peptidylpropyl isomerase B (Cyclophilin B, Cyp), RT/PCR was performed using the primers 5'- CCATCGTGTCATCAAGGACTT and 5'- TTGCCATCCAGCCAGGAGGTC. The expected size of the amplified DNA was 215 bp.

Generation of *Schip1*Δ10 mutant mice

Schip1 mutant mice were generated by deletion of exon 10 of *Schip1*, using a three-lox recombination strategy.

Generation of Schip1$^{flox10/+}$ ES cells

A DNA fragment containing *Schip1* exon 10 surrounded by 3.6 kb endogenous DNA upstream and 5.6 kb endogenous DNA downstream was PCR-amplified in two steps and inserted (using PCR-added *Nsi*I and *Sal*I restriction sites) in a pBR322 vector containing a *NsiI-Sal*I polylinker from pBluescript KS II (Stratagene). A *lox*P sequence was added upstream from exon 10 by PCR. Next, a 2 kb *XmaI-XmaI* fragment containing a floxed PGK*Hygromycin*/*GFP* cassette was inserted 0.8 kb downstream of exon 10 (in the same orientation as the *Schip1* gene).

The *Nsi*I-*Sal1 Schip1-lox10* targeting fragment was electroporated into ES cells (line E14 subclone IB10 (129/Ola)) (Robanus-Maandag et al., 1998) using a Bio-Rad Gene Pulser (0.8kV, 1µF, discharge 0.1 ms, 0.4 cm electrode distance, cells in 200 µl PBS). Electroporated cells were plated on 6 x 60 cm^2 mouse embryonic fibroblasts. After 24 h, hygromycin B 150 µg/ml (Calbiochem) was added for 3 days. Hygromycin-resistant cells were trypsinized and GFP-expressing cells were isolated by flow cytometric analysis and plated on 5 x 96-well microplates. Seven homologous recombinants out of 77 selected clones were identified by long-range PCR analysis. The caryotype of these clones was analyzed. The genomic DNAs were extracted for sequencing and Southern blots were performed to verify 5' and 3' homologous recombination with a probe corresponding to the PGK*Hygromycin*/*GFP* cassette. One clone was then chosen for injection.

Generation and genotyping of Schip1mutant mice

Germline chimeras (*Schip1$^{flox10HygGFP/+}$*) were generated by injection of 10 *Schip1* mutant ES cells into blastocysts and crossed with C57BL/6 mice to produce outbred heterozygous

offspring. The genotypes of all offspring were analyzed by PCR of tail-tip DNA. To generate *Schip1*$^{\Delta 10/+}$ mice, *Schip1*$^{flox10HygGFP/+}$ mice were crossed with *MeuCre* deletor mice (Leneuve et al., 2003). In the derived double transgenic offspring tail DNA the *Schip1*$^{\Delta 10}$ allele was detected by PCR with primers C (5'- CAGACAGCAGACTATCATGGGG) and D (5'- AATGACTGTTCTGAGCACGG) amplifying a 551-bp product and the *Schip1*$^{+}$ allele was detected with primers A (5'- GGGTCACTAAGTTCTCCACATGA) and B (5'- TTGACCACTGAGCCATCTCTGCA) amplifying a 401-bp product. Mosaic mice carrying the *Schip1*$^{\Delta 10}$ allele were subsequently crossed with C57BL/6J mice to segregate the mutant allele and obtain *Schip1*$^{\Delta 10/+}$ mice. Mutant mice were then backcrossed on a C57BL/6J background for at least 10 generations before experiments described here.

Schip1$^{Gt(ROSA)77Sor}$ mice

129S-*Schip1*$^{Gt(ROSA)77Sor}$/J mutant mice (129sv genetic background) were produced by the laboratory of P. Soriano (Chen et al., 2004). They were obtained from the Jackson Laboratory and backcrossed on a C57BL/6J background for at least 10 generations before experiments described here (*Schip1*$^{Gt(ROSA)77Sor}$ or Gt mice). In these mice, the retroviral gene-trap vector ROSAFARY was targeted to intron 5 of *Schip1* (position of the gene-trap defined according to our characterization of the *Schip1* gene). Briefly, this gene-trap vector was designed with a promotor trap module, a *frt*-flanked poly-A trap module, and a promoterless *lacZ-neo* reporter fusion gene, which functions as an artificial 3' terminal exon to intercept and terminate transcription from the targeted promoter. After inserting in an intron of an endogenous gene at a permissive site and in the correct orientation, the promoter trap module and the poly-A trap module can be activated to form fusion transcripts with the 5' or 3' exons, respectively.

Animal procedures

Research was conducted according to national and international guidelines (EC directive 86/609). The laboratory was approved to carry out animal experiments by the *Direction Départementale des Services Vétérinaires de Paris, Service de la Protection et de la Santé Animales et de la Protection de l'Environnement* (licence B75-05-22). The principal investigator had a personal authorization (L Goutebroze, licence 75-1533). Mice were group-housed with *ad libitum* access to food and water and a 12 hour - 12 hour light - dark cycle (light phase onset at 7 a.m.). For staging of embryos, the day of vaginal plug was considered E0.5.

Immunoprecipitations from brain lysates

For preparation of brain extracts, brains were homogenized in a buffer containing 50 mM Tris pH 7.8, 3 mM $MgCl_2$, 320 mM sucrose and Complete protease inhibitors (Roche), using a Heidolph homogenizer. The homogenates were centrifuged 15 min at 4°C at 1000 g. The supernatants were centrifuged at 100 000 g at 4°C for 1 h and the pellets were extracted for 30 min on ice in a buffer containing 10 mM Tris, pH 7.5, 150 mM NaCl, 1 mM EDTA, 1% Triton X-100, 0.1% sodium deoxycholate and Complete protease inhibitors (Roche). The detergent-insoluble material was removed by centrifugation at 100 000 g for 1 h at 4°C. The protein A beads, preincubated with the respective antibody α17141 or HPA, were added to the supernatants and incubated overnight at 4 °C with rotation. Beads were washed with a buffer containing 20 mM Tris pH 7.6, 150 mM NaCl, 0.5% Triton X-100 and Complete protease inhibitors (Roche), precipitated proteins were then loaded on NuPAGE Bis-Tris gels (Invitrogen) and transferred to 0.45 µm Nitrocellulose membranes. Membranes were blocked with TBST buffer (5% dry milk in TBS - 0.1% Tween), 1 h at room temperature, incubated overnight at 4°C with the rabbit antibody α16280 or the chicken antibody α959, and then 1 h

with IRDye^{TM}800CW or IRDye^{TM}680CW secondary antibodies, before development using Odyssey Imaging System (LI-COR Biosciences).

Tissue processing

Adult mice (2 to 3-month old) and E14.5 embryos (for cleaved caspase 3 immunostaining) were deeply anesthetized with pentobarbital (500 mg/kg i.p., Sanofi-Aventis, France) and transcardially perfused with 4% paraformaldehyde (PFA) in 0.12 M phosphate buffer (PB) pH 7.4 for 10 min. E13.5, E14.5, E16.5, E18.5 embryos and P0 newborn mice were rapidly decapitated. Brains (adult and P0 mice; E16.5 and E18.5 embryos) and heads (E13.5 and E14.5 embryos) were fixed or postfixed in 4% PFA overnight at 4°C and cryoprotected in a 30% sucrose/sodium phosphate buffered saline (PBS) solution for 24 h at 4°C. Five hundred µm-thick horizontal sections of adult brains were produced using a vibratome (Leica, France) for phase contrast analysis. For NF160 immunostaining and X-gal staining, 30 µm-thick coronal sections of adult brains were produced using a cryotome (microm KS-34, Thermo Scientific, France) and kept at -20°C in cryoprotectant solution (30% ethylene glycol/30% glycerol/0.12 M PB) until use. For MOG immunostaining and AChE staining, 30 µm-thick sagittal and 40 µm-thick coronal sections of adult brains were produced using a vibratome (Leica, France) and kept at -20°C in the cryoprotectant solution. Brains and heads of P0 mice and embryos were embedded in 7.5% gelatin, 10% sucrose, and 0.12 M PB, snap frozen in isopentane and stored at -20°C until sectioning. Coronal and horizontal 20 µm-thick sections were produced using a cryostat (Microm Microtech, France), thaw mounted onto Superfrost Plus microscope slides (Thermo Fischer Scientific), air-dried and stored at -20°C until use.

Primary cultures of dissociated neurons

The piriform cortex from E14.5 embryos was dissected in ice-cold 0.02 M HEPES in Ca^{2+} /Mg^{2+}-free HBSS (Sigma), and mechanically dissociated after trypsin (2.5 mg/ml) incubation. Dissociated cells were plated on 14 mm-diameter coverslips ($0.3x10^5$ cells/coverslip) coated with poly-L-lysine (0.25 mg/ml) (Sigma, #P7890) and natural mouse laminin (0.01 mg/ml) (Invitrogen, #23017015), and cultured in Neurobasal medium supplemented with B27 (Gibco®) serum-free supplement, Glutamax (Invitrogen), and 1% penicillin/streptomycin at 37°C in presence of 5% CO_2. Neurons were fixed for immunostaining by adding in the medium ½ volume of preheated 8% PFA/20% sucrose in PBS for 20 minutes. For time-lapse imaging, neurons were grown in µ-Slide 8 well-ibiTreat Microscopy Chambers (Ibidi, #80826) at $0.3x10^5$/well coated as described above.

Immunostaining

Fixed neurons/explants on coverslips or tissue sections were incubated in permeabilization/saturation solution PS (0.25% Triton X-100, 5% bovine serum albumin, PBS) or PGT (0.25% Triton X-100, 0.2% gelatin, PBS) for 2 h at room temperature (RT) and then incubated with primary antibodies diluted in the same solution overnight at 4°C. After 3 PBS washes, incubation with Alexa Fluor conjugated-secondary antibodies diluted in PS or PGT solution was performed for 2 h at RT. Then, coverslips and tissue sections were washed again 3 times in PBS and mounted with DAPI-containing Vectashield (Vector Lab). For membrane-bound EPHB2-Fc immunolabeling, fixed neurons were not permeabilized and all incubations were performed in 5% bovine serum albumin/PBS. EPHB2-Fc was detected using a human anti-IgG1 antibody. To visualize F-actin, neurons were incubated for 30 min with Alexa Fluor 488/546/633 conjugated-phalloidin (Molecular Probes) diluted in PBS after secondary antibody incubation.

Acetylcholinesterase staining

Sections were incubated in staining solution (1.7 mM acethylthiocholine iodide, 3 mM copper sulphate, 10 mM sodium citrate, 0.5 mM potassium ferricyanide, 0.2 mM ethopropazine, 0.05 M sodium acetate buffer pH 5.5), rinsed in 0.05 M sodium acetate buffer pH 5.5, deshydrated and mounted with Eukitt® quick-hardening mounting medium (Sigma, #03989).

Nissl coloration

E14.5, E16.5, P0 and adult cryostat coronal sections were treated in sequential baths: 1X 70% ethanol (EtOH), 1X 95% EtOH, 2X 100% EtOH, 1X 95% EtOH, 1X 70% EtOH, 10 seconds/bath. Sections were then stained with cresyl violet (5 mg/ml in 0.6% acetic acid) for 2 minutes, and post-treated in 1X 70% EtOH, 1X 95% EtOH, 2X 100% EtOH, 2X xylene, 10 seconds/bath. Sections were finally mounted with Eukitt® quick-hardening mounting medium.

X-gal staining

Sections were incubated in staining solution (5 mM ferricyanide, 5 mM ferrocyanide, 2 mM $MgCl_2$, 0.1% Triton X-100, 1 mg/ml X-gal, PBS) for 2 h at room temperature, rinsed in PBS, mounted on slides and air-dried overnight. Sections were then incubated in H_20 for 3 minutes, stained in a 0.01% safranine solution, rinsed in H_20 and treated in sequential baths: 1X 70% EtOH, 1X 96% EtOH, 1X 100% EtOH, 2X xylene, 20 seconds/bath. Sections were finally mounted with Eukitt® quick-hardening mounting medium.

BrdU assay

Timed-pregnant heterozygous females at E12.5 received an intraperitoneal injection of 50 mg/kg BrdU (5-bromo-2-deoxyuridine, Sigma). E14.5 or E18.5 embryos were then collected

and tissue prepared as described above. For BrdU immunostaining, sections were permeabilized and blocked in 0.2% Triton X-100/4% BSA/PBS for 2 h at RT. DNA was denaturated with pre-heated 2 N HCl for 40 min at 37°C and sections were then washed in PBS. The following procedure was identical to that described above for immunostaining.

Image acquisitions

Immunolabeled and Nissl stained brain sections (excepted for MOG immunolabeling) were scanned with a Hamamatsu Nanozoomer Digital Pathology 2.0 HT (High Throughput) device (Hamamatsu Photonics, Japan and NDPView Nanozoomer associated software), with fluorescence unit option (L11600-05), and the NanoZoomer's 3-CCD TDI (Time Delay Integration) camera (Hamamatsu Photonics), resolution of 0.23 µm/pixel (40X). MOG-immunolabeled and X-gal-stained sections were imaged with a macroscope MVX10 (Olympus). AChE stained sections were imaged with a Provis light microscope (Olympus). BrdU stained brain sections, immunolabeled neurons and explants were imaged using an epifluorescence DM6000-2 Leica microscope.

For time-lapse imaging, neurons were placed on a motorized stage and maintained at 37°C using a thermostated chamber. Transilluminated time-lapse microscopy was performed using an inverted microscope DMI4000 Leica with a 63x/1.4 N.A. objective (1 acquisition/20 sec during 15 min, z=5 µm, z-step=1 µm).

Visualization of AC axons by fluorescent lipophilic tracer

1,1'-Dioctadecyl-3,3,3',3'-Tetramethylindocarbocyanine Perchlorate ('DiI'; DiIC18(3), Invitrogen, #D-3911) crystals were used to visualize the pathway of AC axons. Brains from E16.5 embryos were fixed for one week in 4% PFA/0.12 M PB. DiI crystals were injected at the base of the olfactory bulb to target the AON/anterior piriform cortex or in the posterior

piriform cortex. Brains were then incubated in PBS for 15 days at 37°C, embedded in 3% agarose/PBS, sliced into 100 µm-thick horizontal sections with vibratome (Leica, France), and imaged with a macroscope MVX10 (Olympus).

In situ hybridization

E13.5, E14.5 embryonic and P0 mouse brains were fixed by immersion with 4% PFA in PBS. Brains were postfixed for 2 h, cryoprotected in 10% sucrose/PBS, frozen in isopentane and stored at -80°C. Serial sections (20 µm) were cut with a cryostat (Microm Microtech, France) and stored at -80°C before hybridization. *Schip1* sense and antisense riboprobes were generated and labeled with digoxigenin-d-UTP by *in vitro* transcription (Roche Diagnostics) from a mouse *Schip1* cDNA encoding the C-terminal residues conserved in all SCHIP1 isoforms (nt[975-1758], GenBank accession number EU163407) cloned in pBluescript II KS+. Antisense riboprobes for guidance molecules were generated by *in vitro* transcription from vectors previously described : NPN2 (Chen et al., 1997); SEMA3F (Falk et al., 2005), generous gift from Pr. A Püschel; EPHB2 (*sek-3*) (Becker et al., 1994). *In situ* hybridizations were performed on tissue sections as described previously (Moreau-Fauvarque et al., 2003). Brain sections were scanned with the Hamamatsu Nanozoomer Digital Pathology (NDP) device as described above.

Statistical analysis

Statistical analyses were performed with StatView software, Abacus. For brain analyses along the antero-posterior axis or during development normally distributed data were subjected to factorial two-way ANOVA with genotype and brain region or age as between-group factors. Significant main effects were further analyzed by post hoc comparisons of means using the Newman–Keuls test. For the other analyses, variables that followed a normal distribution

were subjected to the Student t-test. For variables that did not follow a normal distribution, statistical analyses were carried out using the Mann–Whitney rank sum test to compare quantitative variables. Proportions were compared using the Chi² test. The significance was established at a P-value < 0.05.

SUPPLEMENTARY REFERENCES

Becker, N., Seitanidou, T., Murphy, P., Mattei, M. G., Topilko, P., Nieto, M. A., Wilkinson, D. G., Charnay, P. and Gilardi-Hebenstreit, P. (1994). Several receptor tyrosine kinase genes of the Eph family are segmentally expressed in the developing hindbrain. *Mech Dev* **47**, 3-17.

Chen, H., Chedotal, A., He, Z., Goodman, C. S. and Tessier-Lavigne, M. (1997). Neuropilin-2, a novel member of the neuropilin family, is a high affinity receptor for the semaphorins Sema E and Sema IV but not Sema III. *Neuron* **19**, 547-559.

Chen, W. V., Delrow, J., Corrin, P. D., Frazier, J. P. and Soriano, P. (2004). Identification and validation of PDGF transcriptional targets by microarray-coupled gene-trap mutagenesis. *Nat Genet* **36**, 304-312.

Falk, J., Bechara, A., Fiore, R., Nawabi, H., Zhou, H., Hoyo-Becerra, C., Bozon, M., Rougon, G., Grumet, M., Puschel, A. W. et al. (2005). Dual functional activity of semaphorin 3B is required for positioning the anterior commissure. *Neuron* **48**, 63-75.

Goutebroze, L., Brault, E., Muchardt, C., Camonis, J. and Thomas, G. (2000). Cloning and characterization of SCHIP-1, a novel protein interacting specifically with spliced isoforms and naturally occurring mutant NF2 proteins. *Mol Cell Biol* **20**, 1699-1712.

Leneuve, P., Colnot, S., Hamard, G., Francis, F., Niwa-Kawakita, M., Giovannini, M. and Holzenberger, M. (2003). Cre-mediated germline mosaicism: a new transgenic mouse for the selective removal of residual markers from tri-lox conditional alleles. *Nucleic Acids Res* **31**, e21.

Martin, P. M., Carnaud, M., Garcia del Cano, G., Irondelle, M., Irinopoulou, T., Girault, J. A., Dargent, B. and Goutebroze, L. (2008). Schwannomin-interacting protein-1 isoform IQCJ-SCHIP-1 is a late component of nodes of Ranvier and axon initial segments. *J Neurosci* **28**, 6111-6117.

Moreau-Fauvarque, C., Kumanogoh, A., Camand, E., Jaillard, C., Barbin, G., Boquet, I., Love, C., Jones, E. Y., Kikutani, H., Lubetzki, C. et al. (2003). The transmembrane semaphorin Sema4D/CD100, an inhibitor of axonal growth, is expressed on oligodendrocytes and upregulated after CNS lesion. *J Neurosci* **23**, 9229-9239.

Robanus-Maandag, E., Dekker, M., van der Valk, M., Carrozza, M. L., Jeanny, J. C., Dannenberg, J. H., Berns, A. and te Riele, H. (1998). p107 is a suppressor of retinoblastoma development in pRb-deficient mice. *Genes Dev* **12**, 1599-1609.

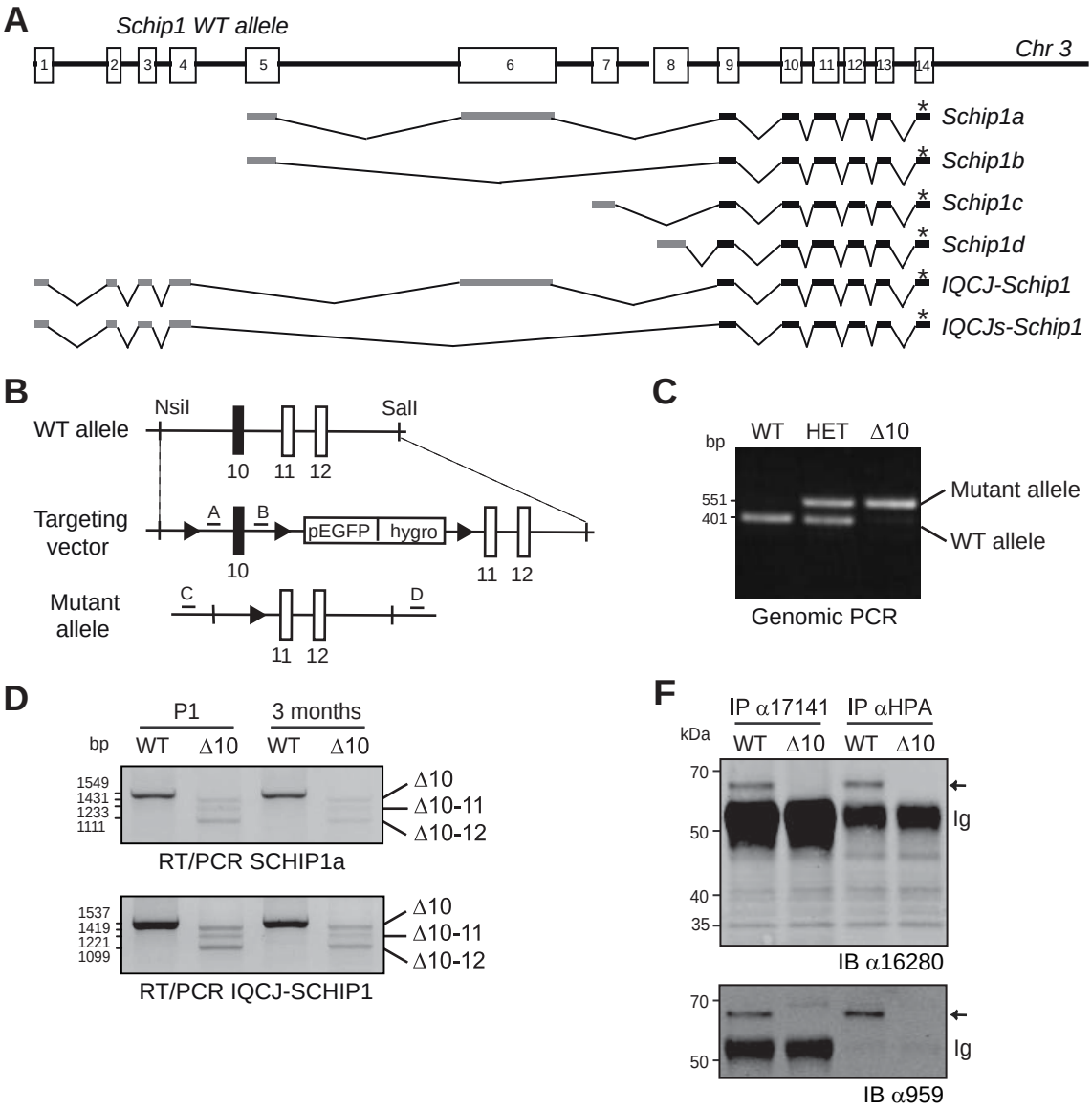

Fig. S1. Generation and characterization of *Schip1* mutant mice.

(A) Schematic representation of mouse *Schip1* isoforms. The *Schip1* gene is composed of 14 exons localized on mouse chromosome 3 and encodes six isoforms expressed in mouse brain. All isoforms differ in their N-terminus and share a C-terminal domain encoded by exons 9 to 14. Black boxes, exons common to all isoforms. Grey boxes, exons specific for one or two isoforms only. *, stop codon. (B) Schematic representation of *Schip1* gene-targeting three-lox strategy. Upper panel, *Schip1* genomic locus including exons 10, 11 and 12. Middle panel,

targeting vector with the three *lox*P sites (black arrowheads) flanking exon 10 and the selection cassette PGK*Hygromycin*/*GFP* (pEGFP/hygro). Lower panel, *Schip1* mutant allele obtained after *in vivo* Cre recombination. Positions of primers used for genotyping (A-D) are indicated. (C) PCR analysis on genomic DNAs of WT, heterozygous (HET) and homozygous *Schip1*Δ10 (Δ10). (D) RT-PCR analysis of SCHIP1a and IQCJ-SCHIP1 mRNAs from WT and Δ10 brains at post-natal day 1 (P1) and 3 months revealing, in mutant brains, low levels of DNA fragments that correspond to cDNAs deleted for the nucleic acids from exon 10 (Δ10) as expected, but also for the nucleic acids from exons 10 and 11 (Δ10-11), and from exons 10, 11 and 12 (Δ10-11-12). (E) Predicted C-terminal amino acid sequences of SCHIP1 mutant proteins. Deletion of exon 10 results in a frameshift, which creates a stop codon in exon 11, leading to the expression of mutant proteins, if any, lacking an 194-residue C-terminal part common to all SCHIP1 isoforms and with a novel unrelated 50-residue extension. Deletions of exons 10-11 and exons 10 to 12 also result in frameshifts, which create stop codons in exons 12 and 13, respectively. Dashed lines substitute for 147 amino acids of WT SCHIP1 proteins. Amino acids encoded by exon 10 are indicated in grey. C-terminal unrelated amino acids encoded by mutant cDNAs Δ10, Δ10-11 and Δ10-12, are indicated in grey and italics. (F) SCHIP1 expression in brain of WT and Δ10 mice. Immunoprecipitations (IP) performed with two different SCHIP1 antibodies, α17141 and HPA, followed by immunoblotting (IB) with two other antibodies α16280 and α959, reveal a protein at the expected molecular weight (65 kDa) for IQCJ-SCHIP1 in WT brain extracts (arrow), which is not detected in Δ10 brain extracts. C-terminal truncated proteins were not detectable in brain extracts from mutant mice (IB α16280). Ig, immunoglobulins.

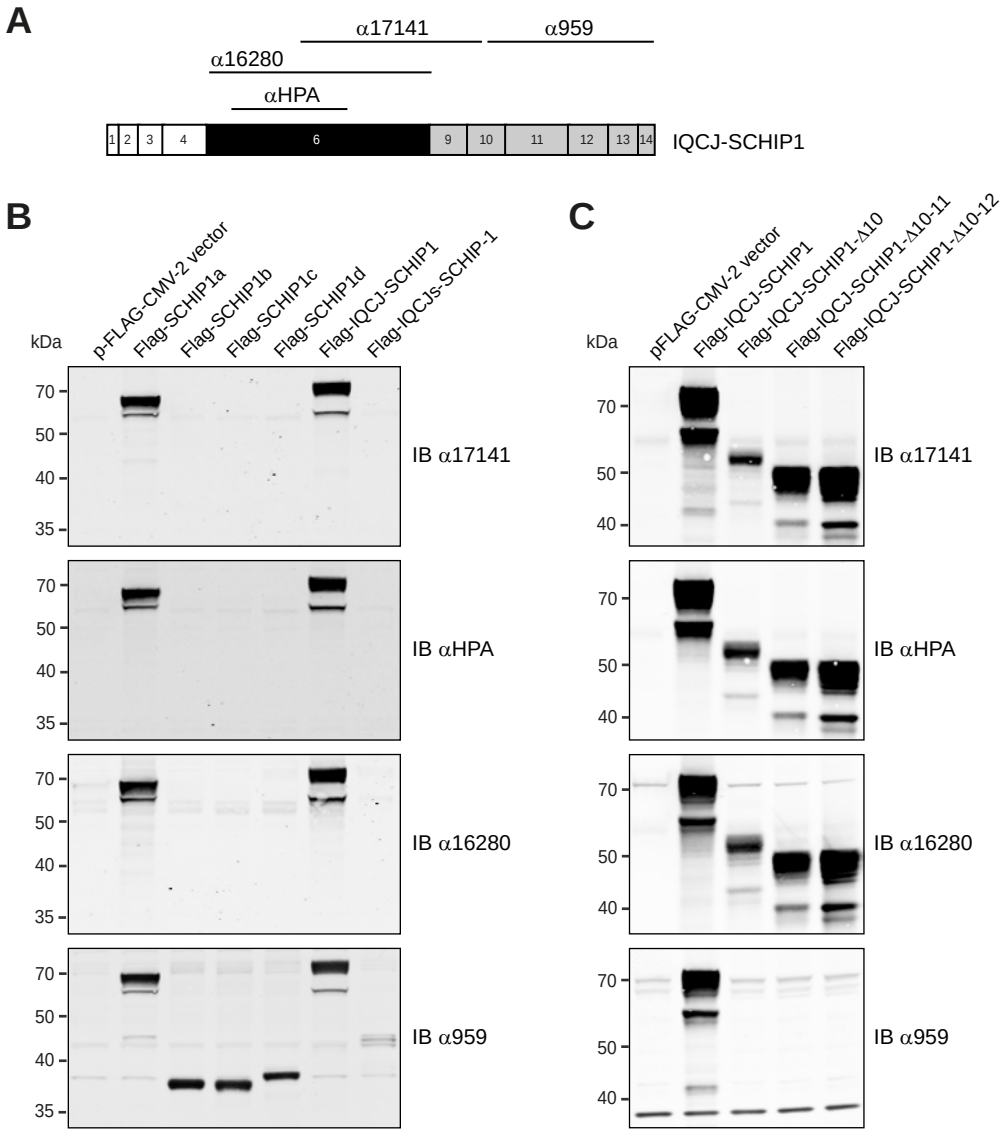

Fig. S2. Characterization of SCHIP1 antibodies. (A) Schematic representation of the antigens used to produce SCHIP1 antibodies (upper lines), aligned along the sequence of the IQCJ-SCHIP1 isoform. Boxes define parts of the protein encoded by the different *Schip1* exons. Grey boxes, exons corresponding to the C-terminal region common to all SCHIP1 isoforms; black box, exon 6 coding for the internal region specific for SCHIP1a and IQCJ-SCHIP1; white boxes, exons 1 to 4 coding for the N-terminal region specific for IQCJ-SCHIP1. (B, C) Characterization of SCHIP1 antibodies by immunoblotting (IB) on lysates from transfected COS-7 cells expressing Flag-tagged SCHIP1 isoforms (Flag-SCHIP1a, Flag-SCHIP1b, Flag-SCHIP1c, Flag-SCHIP1d, Flag-IQCJ-SCHIP1, Flag-IQCJs-SCHIP1) (B), or Flag-tagged IQCJ-SCHIP1 truncated proteins corresponding to the cDNA of IQCJ-SCHIP1 deleted of exon 10 (Flag-IQCJ-SCHIP1-Δ10), exons 10 and 11 (Flag-IQCJ-SCHIP1-Δ10-11), or exons 10 to 12 (Flag-IQCJ-SCHIP1-Δ10-12) (C).

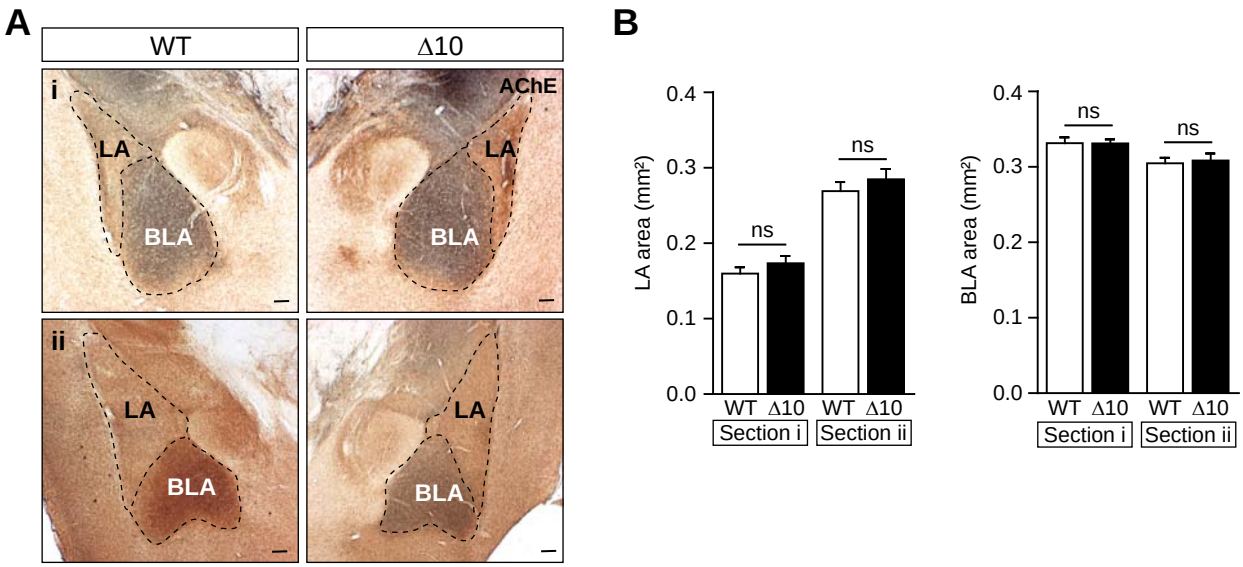

Fig. S3. The size of the amygdala is not affected in *Schip1*Δ10 mice. (A) Acetylcholinesterase (AChE) staining on coronal sections from rostral (i) to caudal (ii) brain regions of adult mice. LA, lateral amygdala; BLA, basolateral amygdala. Black dashed lines show the boundaries of LA and BLA. (B) Quantification of the area of the basolateral and the basal nuclei according to the AChE staining. Data are means±sem. (n=4 animals/genotype; n=3-4 sections/animals; Two-way ANOVA; ns, not significant). Scale bar, 100 µm.

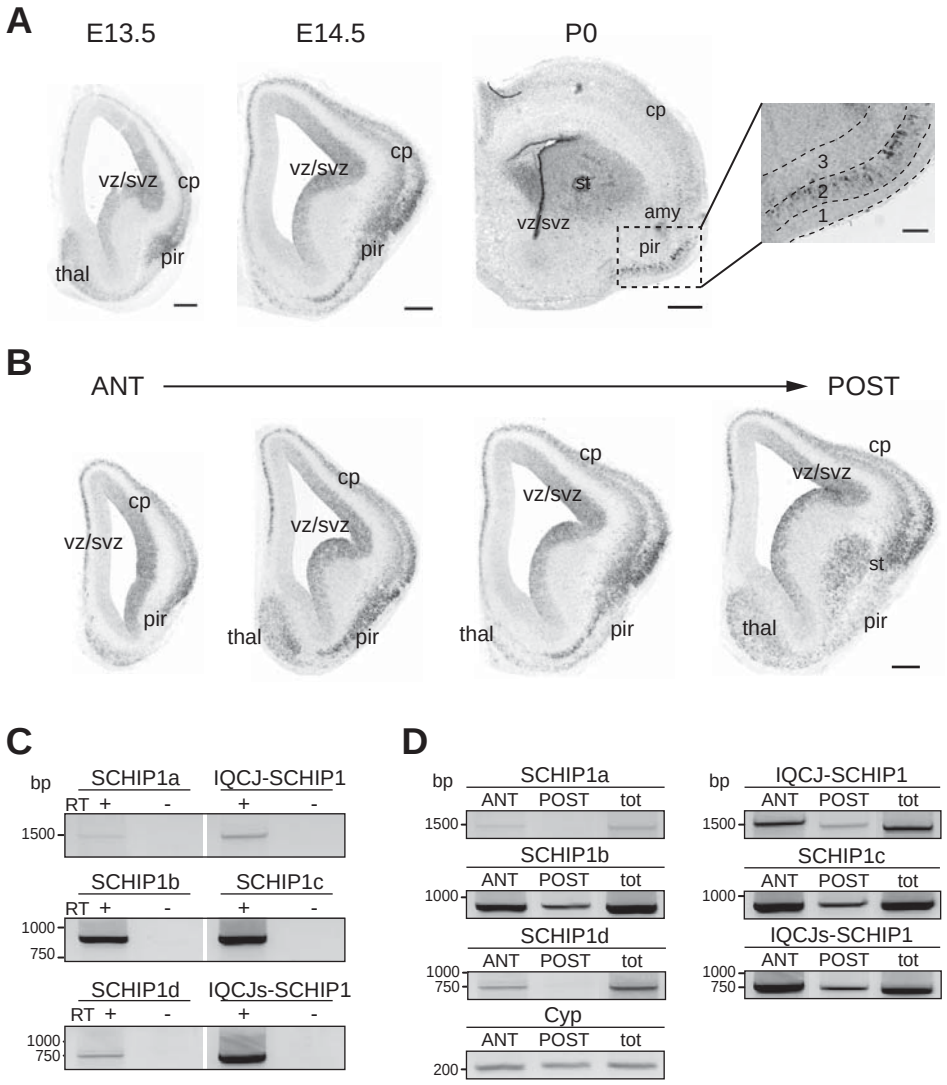

Fig. S4. *Schip1* expression. (A) *In situ* hybridization on WT brain coronal sections at E13.5, E14.5 and P0, using a riboprobe allowing the detection of all *Schip1* mRNA isoforms. Right panel, higher magnification at the level of the piriform cortex at P0. Black dashed lines, boundaries of layers. Pir, piriform cortex; vz/svz, ventricular and subventricular zones; cp, cortical plate; st, striatum; thal, thalamus; amy, amygdala. (B) *In situ* hybridization on WT coronal sections from anterior (ANT) to posterior (POST) regions at E14.5 using a riboprobe allowing the detection of all *Schip1* mRNA isoforms. (C) RT-PCR analysis of the expression of *Schip1* isoforms in WT piriform cortex at E14.5. (D) RT-PCR analysis of the expression of *Schip1* isoforms in WT ANT and POST piriform cortex at E14.5. Cyp, housekeeping gene peptidylpropyl isomerase B. Scale bars, 150 µm.

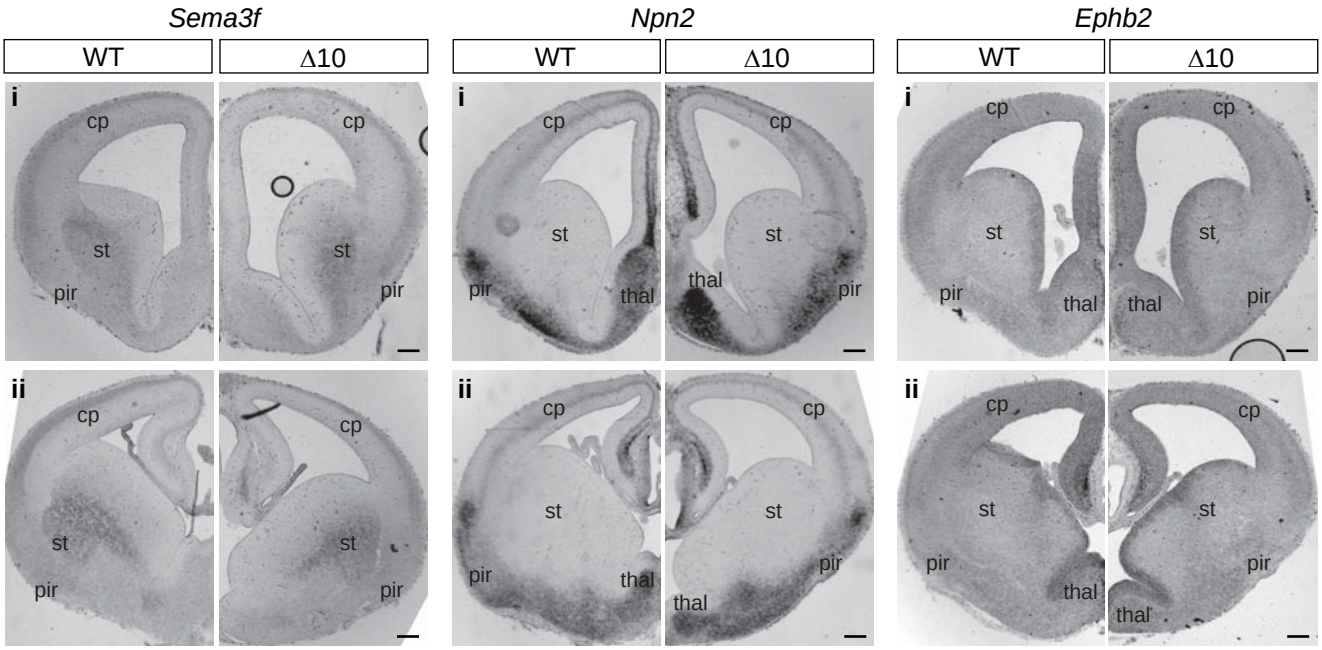

Fig. S5. The expression patterns of *Sema3f*, *Npn2* and *Ephb2* are not affected in *Schip1*Δ10 embryos. *In situ* hybridization on E14.5 brain coronal sections from anterior (i) to posterior (ii) regions using riboprobes allowing the detection of *Sema3f*, *Npn2* and *Ephb2* mRNAs. Pir, piriform cortex; cp, cortical plate; st, striatum; thal, thalamus. Scale bars, 150 µm.

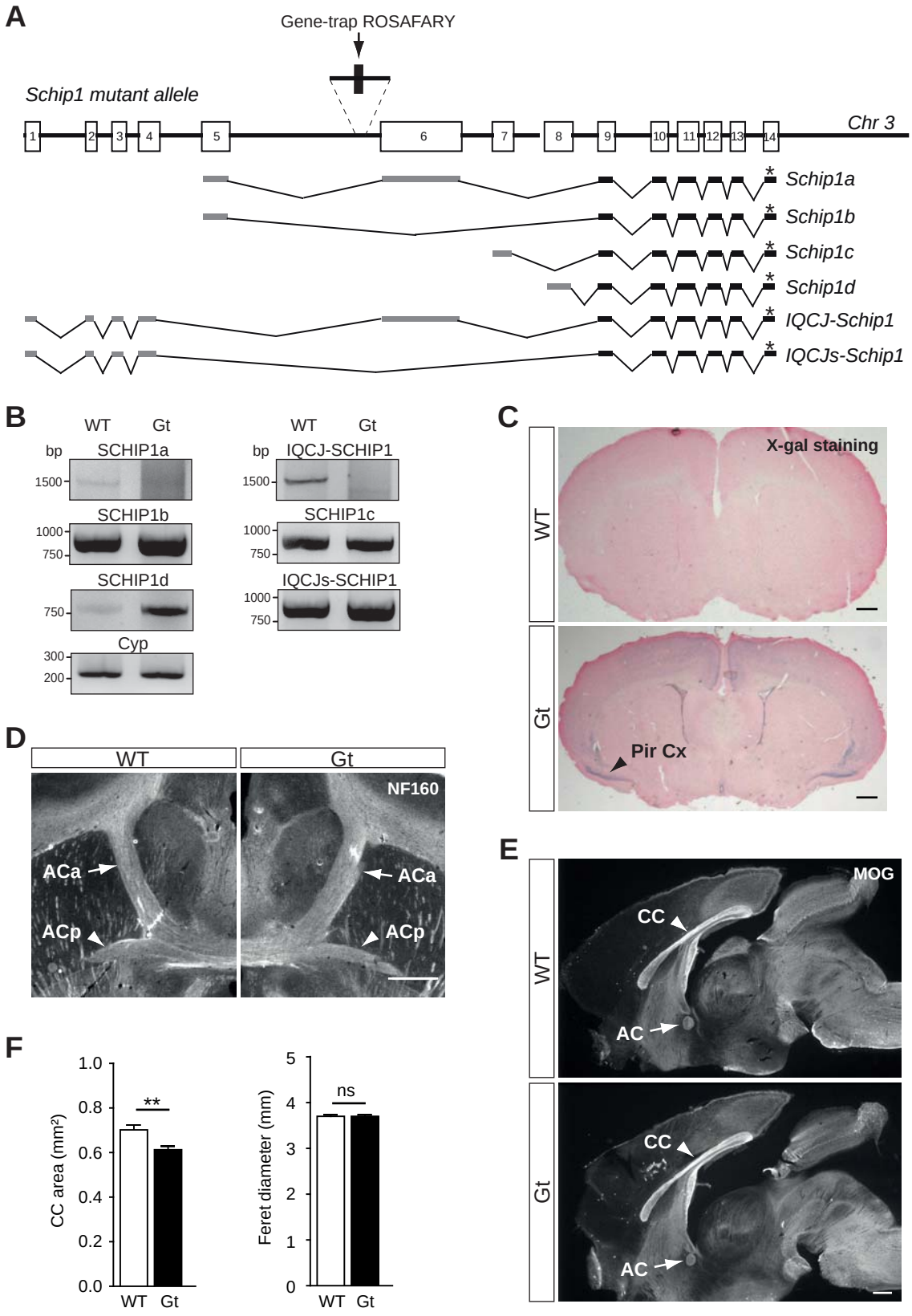

Fig. S6. Characterization of *Schip1*$^{Gt(ROSA)77Sor}$ mice. (A) Schematic representation of *Schip1* gene-trap targeting. The retroviral gene-trap vector ROSAFARY bearing a *lacZ-neo*

reporter fusion gene, was targeted to intron 5 of the *Schip1* gene. (B) Semi-quantitaive RT-PCR analysis of the expression of *Schip1* isoforms in WT and mutant (Gt) adult brains. *Schip1a* and *IQCJ-Schip1* mRNAs are not detectable in Gt mice, whereas the four other isoforms appear overexpressed as compared to WT mice. Cyp, housekeeping gene peptidylpropyl isomerase B. (C) X-gal staining on coronal brain sections detecting the expression of the *lacZ-neo* reporter, notably in the piriform cortex (arrowhead, Pir Cx). (D,E) Gt mice do no present major AC or CC defects. (D) Horizontal brain sections immunolabeled with anti-NF160 antibodies. Arrows, ACa; arrowhead, ACp. (E) Mid-sagittal brain sections immunolabeled with an anti-MOG antibody. Arrows, AC; arrowheads, CC. (F) Quantification of CC area and Feret diameter. Data are means±s.e.m. (n=3 animals/genotype, n=2-3 sections/animal; t-test (G); $^{**}p<0.01$, ns, not significant). Scale bars, 500 µm.

Thickness (µm)	WT	Δ10	P value
P0 ANT neocortex	666.9±26.2	665.8±7.7	*p*=0.9713
P0 POST neocortex	604.2±11.2	586.4±20.6	*p*=0.4669
Adult ANT neocortex	1.131±0.015	1.106±0.017	*p*=0.70
Adult POST neocortex	1.073±0.012	1.031±0.011	*p*=1.00

Table S1: Neocortex thicknesses in newborn and adult mice. Measures were performed on cresyl violet-stained sections at the level of the ACa, named anterior (ANT) region, and at the level of the ACp, named posterior (POST) region. Data are means±s.e.m.; t-test; n=3-5 animals/genotype.

Cell density (x10^3 nuclei/mm^2)	**WT**	**Δ10**	**P value**
ANT piriform cortex layer 2	10.5±0.2	9.9±0.2	*p*=0.14
POST piriform cortex layer 2	9.8±0.2	10.1±0.3	*p*=0.56

Table S2: Piriform cortex layer 2 cell density at P0. Quantification of DAPI stained cells on serial coronal sections. Data are means±s.e.m.; t-test; n=5 animals/genotype.

BrdU+ cell density (cells/mm²)		**WT**	**Δ10**	**P value**
E14.5	ANT piriform cortex	1116±94	1139±80	*p*=0.59
	POST piriform cortex	721±71	769±43	*p*=0.33
E18.5	ANT piriform cortex layer 2	1330±70	1343±56	*p*=0.87
	POST piriform cortex layer 2	1120±53	1143±92	*p*=0.91
Layer 2 thickness (µm)		**WT**	**Δ10**	**P value**
E18.5	ANT piriform cortex layer 2	79.8±4.5	68.7±2.6	*p*=0.098
	POST piriform cortex layer 2	73.0±2.4	63.7±2.2	***p*=0.046***

Table S3: BrdU immunopositive cell density in the piriform cortex at E14.5 and E18.5 and layer 2 thickness at E18.5. Quantification of BrdU immunopositive cell density in the whole piriform cortex at E14.5 and in the piriform cortex layer 2 at E18.5, after BrdU injection in pregnant females at E12.5. Data are means±s.e.m.; t-test; n=3 animals/genotype.

Neuron density (Tuj-1+ cells/field)	**WT**	**Δ10**	**P value**
DIV2	34.1±1.6	33.3±1.1	*p*=0.69
DIV4	40.8±1.5	43.9±2.2	*p*=0.25
Cleaved caspase 3+ cells (%)	**WT**	**Δ10**	**P value**
DIV1	2.8±0.27	2.3±0.39	*p*=0.33
DIV2	4.6±0.69	4.4±0.67	*p*=0.84
DIV4	2.8±0.55	3.0±0.35	*p*=0.70
DIV6	3.8±1.11	2.1±0.33	*p*=0.15

Table S4: Neuron density and percentage of cleaved caspase 3 immunopositive cells in cultures of dissociated piriform cortex neurons. Quantification of Tuj-1 stained cells per acquisition (20X magnification); n=10 acquisitions/embryo, n=5 embryos/genotype (DIV2), n=3 embryos/genotype (DIV4). Percentage of cleaved caspase 3 immunopositive cells per acquisition (20X magnification); n=10 acquisitions/embryo, n=3 embryos/genotype (DIV1), n=5 embryos/genotype (DIV2), n=5-9 embryos/genotype (DIV4), n=3 embryos/genotype (DIV6) . Data are means±s.e.m.; t-test.

Antigen	Species	Reference	Use	Dilution
β3 tubulin	mouse	Covance, #MMS-435P (TUJ1)	IF	1:1000
NF160	mouse	Sigma, #N5264	ICH	1:250
L1CAM	rat	Millipore, #5272	ICH	1:200
MOG	Mouse	Millipore, #5680	ICH	1:50
cleaved caspase 3	rabbit	BD Biosciences, #559565	IF/ICH	1:250
human IgG1	goat	Vector Laboratories, #J0307	IF	1:250
BrdU	rat	ABcys, #117-7513	ICH	1:1000
Flag	rabbit	Sigma, #F7425	IF	1:250
Neuropilin 2	goat	R&D system, #AF567	IF	1:300
digoxigenin (DIG) (alkaline phosphatase-coupled)	sheep	Roche, #11093 274910	ICH	1:2500
Cy3 and Alexa Fluor 488/546/633 conjugated-secondary antibodies	Goat Donkey	Molecular Probes	IF/ICH	1:800
IRDye^{TM}800CW and IRDye^{TM}680CW secondary antibodies	Goat	Rockland Immunochemicals	IB	1:10000

Table S5: Primary and secondary antibody characteristics. IF, immunolabeling on cultured neurons; ICH, immunostaining on tissue; IP, immunoprecipitation; IB, immunoblot.